الجمـــهوريـــة الجـــزائريـــة الديـــمقراطيـــة الشعبيـــة

RÉPUBLIQUE ALGÉRIENNE DÉMOCRATIQUE ET POPULAIRE

وزارة التعـلـيـــم العالـــي والبـــحث العلـــــمي

MINISTÈRE DE L'ENSEIGNEMENT SUPÉRIEUR ET DE LA RECHERCHE SCIENTIFIQUE

جـــامعـة عمـــار ثليـجي بالأغـــواط

UNIVERSITÉ AMAR TELIDJI LAGHOUAT

Faculty of technology

DEPARTMENT: Electrotechnics

OPTION : Automatic and systems

Thesis

In order to obtain a Master's degree in Automation and Systems

Presented by

BOUZIDI Ilyes CHAOUCHE Brahim

Theme

Fault diagnosis of induction machine using AI based on ANFIS method

Defended publicly before a jury composed of:

Full name	Grade	Quality
Mrs KOUZI katia	Pr	President
Mrs ABDEREZZAK Hadjer	MCA	Examiner
Mr BESSEDIK Sid Ahmed	Pr	Supervisor
Mr AMEUR Aissa	Pr	Co- Supervisor

Academic Year 2025 / 2026

Acknowledgments

Our first thanks go to our thesis supervisors, Mr. ***BESSEDIK Sid Ahmed*** *and Mr.* ***AMEUR Aissa****, who agreed to supervise us during this work. We are deeply grateful for their support, their assistance, and the trust they placed in us; may they find here the expression of our sincere gratitude.*

We would also like to extend our warmest thanks to Mrs. ***KOUZI Katia****, professor at the university of Laghouat, for the great honor she has given us by chairing the defense jury. We also thank Mrs.* ***ABDEREZZAK Hadjer****, associate professor at the university of Laghouat, for agreeing to evaluate this work.*

We thank everyone who contributed, directly or indirectly, to the successful completion of this work.

Finally, we wish to express our deepest gratitude to our families, who have always supported us, to everyone who participated in the realization of this thesis, and to all the teachers who have contributed to our education.

Dedication

To my parents, the root of my existence, whose silent sacrifices, shared late nights, and reassuring words have shaped my journey.

To my aunts, my benevolent stars, who guided me on the path of hard work and perseverance.

To my brother and sister, my companions along the way and faithful pillars of support, whose presence, advice, and humor brightened my hardest days.

To my two grandmothers, whose memory and life lessons continue to inspire every step of my journey.

May these pages reflect the strength of your faith in me.

Thank you for making this dream possible. Merci d'avoir rendu possible ce rêve.

Bouzidi Ilyes

Abstract

The induction machine is widely used in industry due to its simplicity, robustness, and low cost. It also requires minimal maintenance and provides high performance. However, during operation, it may be subjected to internal or external stresses. These stresses can lead to faults and operational failures. Such failures often cause costly production shutdowns. They may also result in significant material and financial losses. Therefore, it is essential to develop efficient and fast diagnostic methods. This thesis investigates the use of the ANFIS neuro-fuzzy approach for stator fault diagnosis. This method enables early fault detection and accurate fault localization. As a result, it improves machine reliability and reduces industrial losses.

Keywords: *Asynchronous machine, inter-turn short-circuit, Adaptive Neuro-Fuzzy Inference System (ANFIS), fault diagnosis.*

ملخص

تُستخدم الآلة غير المتزامنة على نطاق واسع في المجال الصناعي بفضل بساطتها ومتانتها وتكلفتها المنخفضة. كما أنها تتطلب صيانة قليلة وتتميز بأداء عالٍ. ومع ذلك، قد تتعرض أثناء التشغيل لإجهادات داخلية أو خارجية. يمكن أن تؤدي هذه الإجهادات إلى حدوث أعطال واختلالات في التشغيل. وغالبًا ما تتسبب هذه الأعطال في توقف الإنتاج بشكل مكلف. كما قد تؤدي إلى خسائر مادية ومالية كبيرة. لذلك، أصبح من الضروري تطوير طرق تشخيص فعالة وسريعة. تتناول هذه المذكرة دراسة استخدام منهجية ANFIS العصبية الضبابية لتشخيص أعطال الجزء الثابت. تسمح هذه الطريقة بالكشف المبكر عن الأعطال وتحديد مواقعها بدقة. وبالتالي، فإنها تساهم في تحسين موثوقية الآلة وتقليل الخسائر الصناعية.

الكلمات المفتاحية: الآلة غير المتزامنة، قصر بين اللفات، نظام الاستدلال العصبوني الضبابي التكيفي (ANFIS)، تشخيص الأعطال.

Résumé

La machine asynchrone est largement utilisée dans l'industrie grâce à sa simplicité, sa robustesse et son faible coût. Elle nécessite également peu d'entretien et offre de bonnes performances énergétiques. Cependant, durant son fonctionnement, elle peut subir des contraintes internes ou externes. Ces contraintes peuvent provoquer des défauts et des dysfonctionnements. Les pannes entraînent souvent des arrêts de production coûteux. Elles peuvent aussi générer des pertes matérielles et financières importantes. Il est donc nécessaire de développer des méthodes de diagnostic efficaces et rapides. Ce mémoire étudie l'utilisation de l'approche neuro-floue ANFIS pour le diagnostic des défauts statoriques. Cette méthode permet de détecter et de localiser les défauts dès leur apparition. Ainsi, elle contribue à améliorer la fiabilité de la machine et à réduire les pertes industrielles.

Mots-clés : *Machine asynchrone, court-circuit entre spires, Système d'inférence neuro-flou adaptatif (ANFIS), diagnostic de défauts.*

List of Symbols

Chapter I — Machine Structure and Operating Principle	
Ns	Synchronous speed (rpm)
f	Supply frequency (Hz)
P	Number of poles
s	Slip
Nr	Actual rotor speed (rpm)
fr	Rotor cage current frequency
Chapter I — Fault Signature Frequencies	
fbrb	Broken rotor bar sideband frequencies
fs	Supply fundamental frequency (Hz)
k	Harmonic index (k = 1, 2, 3, …)
fecc	Eccentricity harmonic frequencies in the stator current
R	Rotor slot count
nd	Eccentricity order
P	Pole-pair count
V	Stator harmonic order (v = 1, 3, 5, …)
BPFO	Ball Pass Frequency, Outer race
BPFI	Ball Pass Frequency, Inner race
BSF	Ball Spin Frequency
FTF	Fundamental Train Frequency
Chapter I — Insulation Thermal Model	
L(T)	Insulation lifetime at temperature T
A	Pre-exponential material constant
Ea	Activation energy of the dominant degradation reaction (eV)
kB	Boltzmann's constant (8.617×10^{-5} eV/K)
Ath	Cumulative thermal ageing index
Trated	Rated insulation class temperature
Chapter II — Three-Phase Machine Model	
Us , *Ur*	Stator and rotor voltage vectors
is , *ir*	Stator and rotor current vectors
Φs , *Φr*	Stator and rotor flux linkage vectors

Rs , Rr	Stator and rotor resistance matrices
Lsp , Lrp	Stator and rotor self-inductances
Ms	Mutual inductance between two stator phases
Mr	Mutual inductance between two rotor phases
Chapter II — Park Transformation and dq Model	
$P(\theta s)$	Park transformation matrix
Θs	Reference frame angle : $\theta s = \int \omega s \, dt$
Ωs	Angular speed of the reference frame (rad/s)
Ωe	Electrical supply angular frequency (rad/s)
Vds , Vqs	Direct- and quadrature-axis stator voltages
Vdr , Vqr	Direct- and quadrature-axis rotor voltages
Rs	Stator resistance
Rr	Rotor resistance
ids , iqs	Direct- and quadrature-axis stator currents
idr , iqr	Direct- and quadrature-axis rotor currents
φds , φqs	Direct- and quadrature-axis stator flux linkages
φdr , φqr	Direct- and quadrature-axis rotor flux linkages
Ωr	Electrical rotor speed : $\omega r = P \cdot \Omega$ (rad/s)
Ω	Mechanical rotor speed (rad/s)
Ls	Total stator inductance : $Ls = lfs + Lm$
Lr	Total rotor inductance : $Lr = lfr + Lm$
Lm	Magnetising inductance
lfs , lfr	Stator and rotor leakage inductances
Σ	Total leakage factor : $\sigma = 1 - Lm^2 / (Ls \cdot Lr)$
Chapter II — Mechanical Equation	
J	Total moment of inertia of the rotor and load (kg·m²)
Cem	Electromagnetic torque (N·m)
Cr	Load resistive torque (N·m)
F	Viscous friction coefficient (N·m·s/rad)
Chapter II — Stator Inter-Turn Short-Circuit Fault Model	
Rcc	Fault resistance (short-circuit contact resistance)
μcc	Number of shorted turns

N	Total number of turns in the affected coil
μ	Short-circuit ratio fraction of shorted turns bypassed
Icc	Circulating fault current
Vsa	Phase A stator voltage
Isa	Phase A stator current
φsam	Mutual flux linkage component of phase A
$iccd$, $iccq$	d- and q-axis projections of the fault current Icc
Chapter III — ANFIS Layer Parameters	
x , y	Input variables of the ANFIS system
$\mu A(x)$, $\mu B(y)$	Membership function values for inputs x and y
a , b , c	Premise parameters tuned by backpropagation
Wi	Firing strength of fuzzy rule i
$RMSE$	Root Mean Squared Error
$\bar{w}i$	Normalized firing strength of fuzzy rule i
Fi	Consequent function of rule i ： fi = pi·x + qi·y + ri
p , q , r	Consequent parameters tuned by Least Squares Estimation (LSE)
$O_1 \ldots O_5$	Outputs of ANFIS layers 1 through 5

List of figures and tables

List of figures

Figure 1: Transverse cross-section of a squirrel-cage induction motor ……...……4
Figure 2:Three-dimensional perspective of a squirrel-cage rotor 5
Figure 3:Comparison of induction motor failure distributions 8
Figure 4:Inter-turn short-circuit Fault……..……;……9
Figure 5:Rotor cage cross-section showing a broken bar 11
Figure 6:Three types of rotor eccentricity……..……;……..12
Figure 7 :Motor Current Signature Analysis (MCSA)..... 14
Figure 8:Bearing condition monitoring and characteristic defect frequencies 15
Figure 9:Five-layer ANFIS architecture and functional layers tuned by hybrid training. 19
Figure 10:Schematic representation of a three-phase induction machine. 24
Figure 11:Simulink/MATLAB Modeling of a Squirrel-Cage Induction Motor..... 30
Figure 12:Evolution of Stator Phase Currents During Startup and Under Load Conditions..... 32
Figure 13:Evolution of Rotational Speed During Startup and Under Load Conditions 33
Figure 14:Evolution of Electromagnetic Torque During Startup and Under Load Conditions. 34
Figure 15:Modeling a Squirrel-Cage Induction Motor with Stator Faults in MATLAB 35
Figure 16:Three-phase stator currents in the presence of the inter-turn short-circuit fault..... 36
Figure 17:Electromagnetic torque Cem (N·m) in the presence of the stator fault..... 37
Figure 18: Rotor angular speed Ω (rad/s) in the presence of the stator fault..... 38
Figure 19 :Artificial Neural Network Architecture for Induction Machine Fault Diagnosis 40
Figure 20:Block Diagram of a Fuzzy Inference System (FIS) for IM Fault Diagnosis……41
Figure 21:Fuzzy Membership Functions for Induction Machine Diagnostic Features..... 42
Figure 22:ANFIS Architecture: 5-Layer Adaptive Neuro-Fuzzy Inference System 44
Figure 23:ANFIS Membership Function Adaptation and Output Surface 46
Figure 24:Gaussian membership functions for Input 1 (first stator current feature) 51
Figure 25:Gaussian membership functions for Input 2 (second stator current feature)..... 51
Figure 26:Comparison of ANFIS output and target values during the training phase 52
Figure 27:Comparison of ANFIS output and target values during the testing phase 54
Figure 28:Absolute error of the ANFIS model on the training dataset..... 55
Figure 29:3D surface of the ANFIS model output as a function of Input 1 and Input 2..... 56

List of tables

Table 1:Taxonomy of induction machine fault types classified by origin and category..... 7
Table 2:Comparative summary of the three main diagnostic method families 20
Table 3:Attribute comparison of principal AI diagnostic methods for induction machines 20
Table 4:ANFIS hybrid learning algorithm 46
Table 5:Summary of the dataset used for ANFIS training and testing 49
Table 6:ANFIS configuration and training parameters..... 50
Table 7:ANFIS model performance summary 57

Summary

General Introduction 1

CHAPTER I: **Diagnostic Methods for Asynchronous Induction Machines**

I.1 Introduction 3
I.2 Structure of the Asynchronous Induction Machine 4
I.2.1 The Stator 4
I.2.2 The Squirrel-Cage Rotor 5
I.2.3 Mechanical Components 6
I.2.4 Operating Principle and the Slip 6
I.3 Failure Modes in Asynchronous Machines 7
I.3.1 Statistical Overview of Failure Distribution 7
I.3.2 Stator Winding Faults 8
I.3.2.1 Insulation Degradation Mechanisms 8
I.3.2.2 Inter-Turn Short Circuit 9
I.3.2.3 Phase to Phase and Phase to Ground Faults 10
I.3.3 Rotor Faults 10
I.3.3.1 Broken Rotor Bars 11
I.3.3.2 End-Ring Cracks 11
I.3.3.3 Rotor Eccentricity 12
I.3.4 Bearing Faults 13
I.3.5 Environmental and External Stresses 13
I.4 Diagnostic Methods for Induction Machines 14
I.4.1 Signal-Based Methods 14
I.4.1.1 Motor Current Signature Analysis (MCSA) 14
I.4.1.2 Vibration Monitoring 15
I.4.1.3 The Park Vector Approach 16
I.4.1.4 Thermal and Stray-Flux Monitoring 16
I.4.2 Model-Based Diagnostic Methods 16
I.4.3 Artificial Intelligence-Based Methods 18
I.4.3.1 Artificial Neural Networks 18
I.4.3.2 Fuzzy Logic Systems 18
I.4.3.3 Adaptive Neuro-Fuzzy Inference Systems (ANFIS) 19
I.5 Conclusion 21

CHAPTER II : Modeling of the squirrel-cage asynchronous machine

II.1 Introduction.....23
II.2 Mathematical Model of the Healthy Machine.....23
II.2.1 Electrical Equations of the Induction Motor.....23
II.2.2 The Park Transformation and the dq Model.....26
II.2.2.1 Principle of the Park Transformation.....26
II.2.2.2 Voltage Equations in the dq Reference Frame.....26
II.2.2.2 Flux Linkage Equations in the dq Frame.....27
II.2.2.3 State-Space Formulation.....27
II.3 Mechanical Equation of Motion.....28
II.4 Modeling of the Stator Inter-Turn Short-Circuit Fault.....29
II.4.1Physical Description of the Fault..... 29
II.4.2 Modified Voltage Equations with the Fault.....29
II.4.3 Effect of the Fault on the dq Model.....29
II.5 Simulink Implementation (Healthy Machine).....30
II.5.1 Simulation Results for healthy Operation.....31
II.5.2 Stator Currents for healthy Operation.....31
II.5.3 Electromagnetic Torque for healthy Operation.....32
II.5.4 Rotor Speed for healthy Operation.....33
II.6 Simulink Implementation (Machine with Stator Fault).....34
II.6.1 Simulation Results Machine with Stator Fault.....35
II.6.2 Stator Currents Faulty Operation.....36
II.6.3 Electromagnetic Torque Faulty Operation.....37
II.6.4 Rotor Speed Faulty Operation.....37
II.7 conclusion.....38

CHAPTER III : Fault diagnosis of ASM using the ANFIS approach

III.1 Introduction.....39
III.2 Artificial Neural Network (ANN) Method.....39
III.2.1 Overview and Motivation.....39
III.2.2 ANN Architecture 40
III.3 Fuzzy Logic (FL) Method.....40
III.3.1 Overview and Theoretical Background 40
III.3.2 Fuzzy Inference System (FIS) Architecture.....41
III.3.3 Membership Functions.....41
III.3.4 Rule Base and Inference Engine.....42

III.3.5 Defuzzification……43
III.3.6 Advantages and Limitations……43
III.4 Adaptive Neuro-Fuzzy Inference System (ANFIS) ……43
III.4.1 Concept and Motivation……43
III.4.2 ANFIS 5-Layer Architecture……44
III.4.3 Membership Function Adaptation and Output Surface ……..……46
III.4.4 Hybrid Learning Algorithm……46
III.4.5 Advantages and Limitations……47
III.5 Simulation results of the stator fault model……...47
III.5.1 Dataset Description and Preprocessing……48
III.5.2 ANFIS Model Configuration and Training Parameters ..……49
III.5.3 Input Membership Functions……50
III.5.4 Training Phase Results……..52
III.5.5 Testing Phase Results……54
III.5.6 Absolute Training Error Analysis…….……55
III.5.7 Input–Output Surface of the Trained ANFIS Model……56
III.5.8 Performance Summary and Comparative Evaluation……57
III.5.9 Discussion……58
III.6. Conclusion..……59
General conclusion ……61

General introduction

The squirrel-cage induction machine is the most widely used electromechanical energy converter in the industrial sector, accounting for approximately 70% of all electric motors worldwide. Its dominance is justified by a unique combination of key advantages, including a simple brush-free rotor design, exceptional mechanical robustness, low manufacturing cost, minimal maintenance requirements, and high operational reliability across diverse environments.

However, any unexpected failure can trigger cascading consequences, causing unscheduled downtime, production losses, secondary equipment damage, and severe safety hazards. Despite its durability, the machine is subjected to severe electrical, mechanical, and environmental stresses. Statistical surveys consistently show that bearing failures account for 40 to 50% of breakdowns, stator winding faults for 30 to 40%, and rotor defects for 5 to 10%. Among stator faults, the inter-turn short circuit is the most critical and prevalent incipient failure. It originates from localized insulation degradation between adjacent turns and, if undetected, propagates progressively, escalating into catastrophic phase-to-phase or phase-to-ground faults. Consequently, continuous condition monitoring and early diagnosis are vital research axes.

Traditional diagnostic methods, such as Motor Current Signature Analysis (MCSA) and model-based approaches, have shown effectiveness but suffer from well-identified limitations. These include a low sensitivity to incipient faults and a strong dependence on expert interpretation. To overcome these challenges, artificial intelligence techniques have emerged as a powerful path. Among them, the Adaptive Neuro-Fuzzy Inference System (ANFIS) offers an optimized solution. ANFIS combines the adaptive learning capabilities of neural networks with the transparent interpretability of fuzzy logic, enabling automatic tuning of its membership functions.

This integration ensures a highly accurate, robust, and automated fault diagnosis system, making it perfectly suited for modern predictive maintenance and reliable industrial deployment.

The objective of this work is to design an ANFIS-based diagnostic approach for the detection and severity quantification of stator inter-turn short-circuit faults in squirrel-cage induction machines. The manuscript is organized into three chapters:

The first chapter provides an introduction to fault diagnosis, beginning with a brief review of the technological construction of the squirrel-cage induction machine. This is followed by a comprehensive classification of the various faults that can affect each component of the machine, detailing their causes, effects, and statistical studies. Finally, a synthesis of the methods and techniques used for fault detection is presented.

The second chapter is dedicated to developing models of the induction machine under both healthy and faulty operating conditions, as well as analyzing the various simulated variables of the machine. After studying the healthy behavior of the machine, understanding its faulty operating characteristics becomes essential. Recognizing fault signatures during condition monitoring is crucial and constitutes a key element in developing effective fault detection and localization techniques. In this work, we focus specifically on stator inter-turn short-circuit faults.

The third chapter focuses on the application of the ANFIS (Adaptive Network Based Fuzzy Inference System) neuro-fuzzy approach to detect stator inter-turn short-circuit faults. Finally, this thesis concludes with a general conclusion that summarizes the work accomplished.

CHAPTER I

State of the Art: Diagnostic Methods for Asynchronous Induction Machines

I.1 Introduction

The squirrel-cage induction machine is the dominant electromechanical energy converter in modern industry due to its robust, brush-free design, cost-effectiveness, and low maintenance needs across diverse applications. However, these machines are susceptible to progressive degradation from electrical, thermal, mechanical, and environmental stresses such as stator insulation breakdown, rotor cage cracking, bearing wear, and eccentricity which, if left unchecked, can lead to catastrophic failures and severe financial losses. To mitigate these risks, industry has adopted Condition-Based Maintenance (CBM), an evidence-driven strategy that triggers interventions only when measurable deterioration reaches a specific threshold. Implementing CBM requires reliable, non-intrusive monitoring systems capable of early fault detection, a need that has driven forty years of research spanning signal processing, physics-based modeling, and artificial intelligence. To establish the theoretical foundation for these diagnostic methods, this chapter outlines the physical structure and operating principles of the asynchronous machine, systematically reviews its primary failure modes and their consequences, surveys current diagnostic techniques, and concludes by justifying the specific diagnostic approach adopted in this thesis [1].

I.2 Structure of the Asynchronous Induction Machine

An asynchronous machine is fundamentally composed of two electromagnetic subassemblies the stator and the rotor separated by a narrow air gap, together with mechanical components that provide support, containment, and thermal management. Figure I.1 shows a transverse cross-section of a four-pole squirrel-cage machine illustrating the concentric arrangement of its principal components.

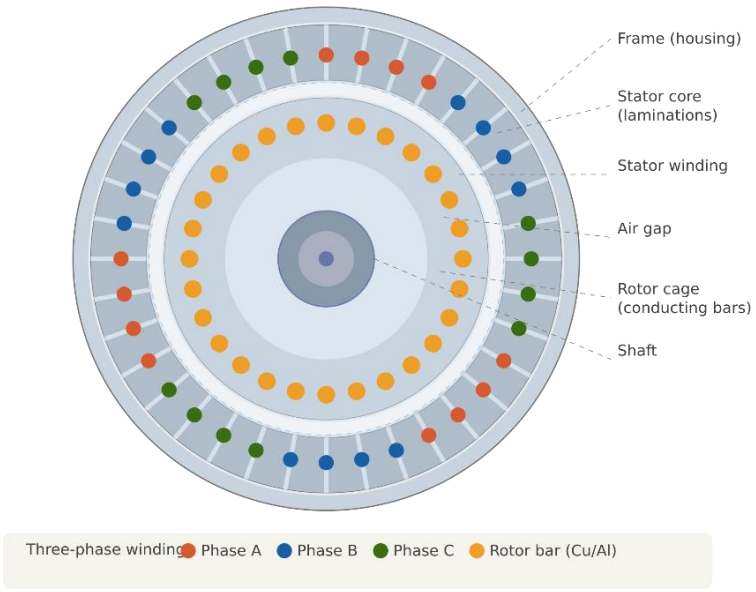


Figure 1 Transverse cross-section of a squirrel-cage induction motor

I.2.1 The Stator

The stator constitutes the fixed outer structure of the machine. Its magnetic circuit is assembled by stacking thin silicon-steel laminations, typically 0.35 to 0.65 mm thick, that are individually coated with an insulating varnish to suppress eddy currents and thereby minimise core losses. Rectangular slots machined into the inner bore of the lamination stack receive the three-phase winding. Each conductor is insulated from its neighbours and from the core by a multilayer system comprising slot liners, inter-turn insulation film, and vacuum-pressure-impregnated resin.

When a balanced three-phase supply is connected to the stator terminals, the three phase currents equal in amplitude and displaced by 120° in time combine to produce a resultant magnetomotive force (MMF) that rotates in the air gap at the synchronous speed:

$$Ns = 120\, f / P \qquad (I.1)$$

where f is the supply frequency in hertz and P is the number of poles. For a standard four-pole machine on a 50 Hz supply, Ns = 1500 rpm. The rotating MMF induces voltages in the rotor conductors and is the primary driver of the electromechanical energy conversion process.

The stator winding insulation system is the subcomponent most critical to long- term machine reliability. It is simultaneously exposed to the highest voltage stress, the highest operating temperature, and repeated mechanical vibration a combination that accelerates deterioration more rapidly than any single stress acting in isolation. Statistical surveys consistently show that insulation degradation is the initiating mechanism for the majority of stator-related failures [1].

I.2.2 The Squirrel-Cage Rotor

The rotor is the rotating inner element of the machine. In the squirrel-cage configuration, which accounts for the large majority of industrial induction motor installations, the rotor lamination stack carries conductive bars of aluminium in small machines and of copper in large machines embedded in slots on its outer cylindrical surface. At each axial end of the stack, all bars are short-circuited by a conducting end ring, forming the cage structure that gives the design its name. Figure 2 shows the three-dimensional perspective of the cage, with bars, end rings, and shaft clearly visible.

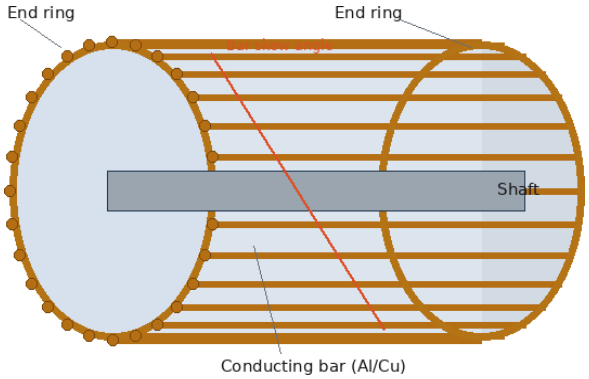


Figure 2 Three-dimensional perspective of a squirrel-cage rotor

Because the cage bars are short-circuited through the end rings, rotor currents are induced automatically whenever a relative velocity exists between the rotating stator field and the rotor conductors no external rotor circuit connection is required. This self-contained electrical circuit eliminates the brushgear and slip-rings needed by

wound-rotor and DC machines, significantly reducing maintenance requirements and improving reliability. The bars are given a helical skew of approximately one slot pitch to suppress slot-harmonic torque pulsations and reduce acoustic noise during operation [1].

I.2.4 Mechanical Components

The shaft, machined from medium-carbon steel, transmits the electromagnetic torque produced in the air gap to the mechanical load. It is supported by two rolling- element bearings housed in the machine end shields. Deep-groove ball bearings are the standard choice for small and medium frame sizes, while cylindrical-roller or angular- contact bearings are used when the application imposes high radial loads or significant axial forces. The Totally Enclosed Fan-Cooled (TEFC) design in which an external fan mounted on the non-drive end of the shaft forces ambient air over longitudinal fins on the outer frame surface is the most widely produced configuration [4].

I.2.5 Operating Principle and the Slip

The operating principle of the induction machine is grounded in Faraday's law. The stator rotating field sweeps across the rotor bars, inducing an EMF in each bar proportional to the rate of flux linkage change. Since the bars are short-circuited, the induced EMF drives currents through the cage circuit. The Lorentz interaction between these rotor currents and the stator field produces an electromagnetic torque that accelerates the rotor in the direction of field rotation.

The rotor always rotates at a speed slightly below the synchronous speed: without this speed difference the slip there would be no flux linkage change and hence no induced rotor current. The dimensionless slip is defined as:

$$s = (Ns - Nr)/Ns \quad \text{(I.2)}$$

where Nr is the actual rotor speed in rpm. Under rated full-load conditions, slip typically lies in the range 0.02 to 0.08 for standard squirrel-cage machines. The rotor cage currents flow at frequency $fr = s \cdot f$, which is a few hertz at rated load a fact exploited directly in rotor fault diagnosis [1].

I.3 Failure Modes in Asynchronous Machines

A clear understanding of the physical origin, progression, and observable consequences of each failure mode is a prerequisite for designing an effective diagnostic system. Table I.1 provides a structured taxonomy of the principal fault types classified by their origin.

Table 1 Taxonomy of induction machine fault types classified by origin and category

Origin	Category	Representative fault types
Internal	Electrical	Inter-turn short circuit, phase-to-phase fault, phase-to-ground fault, rotor bar breakage, end-ring crack
Internal	Mechanical	Bearing failure, rotor eccentricity, shaft misalignment, rotor-to-stator contact
Internal	Magnetic	Cracked or shorted laminations, local saturation asymmetry, non-uniform air gap
External	Supply network	Voltage unbalance, supply harmonics, converter- induced surge overvoltages, frequent starts
External	Load	Mechanical overload, pulsating torque, vibrations transmitted from the driven machine
External	Environment	Excessive ambient temperature, humidity ingress, dust, chemical contamination

I.3.1 Statistical Overview of Failure Distribution

Industrial surveys conducted over four decades on large squirrel-cage motors in petrochemical and manufacturing environments provide quantitative estimates of the relative frequency of each fault category. Figure I.3 presents the failure distribution reported by Thomson (1999) and Bonnett (2008), the two most widely cited studies in the diagnostic literature [4].

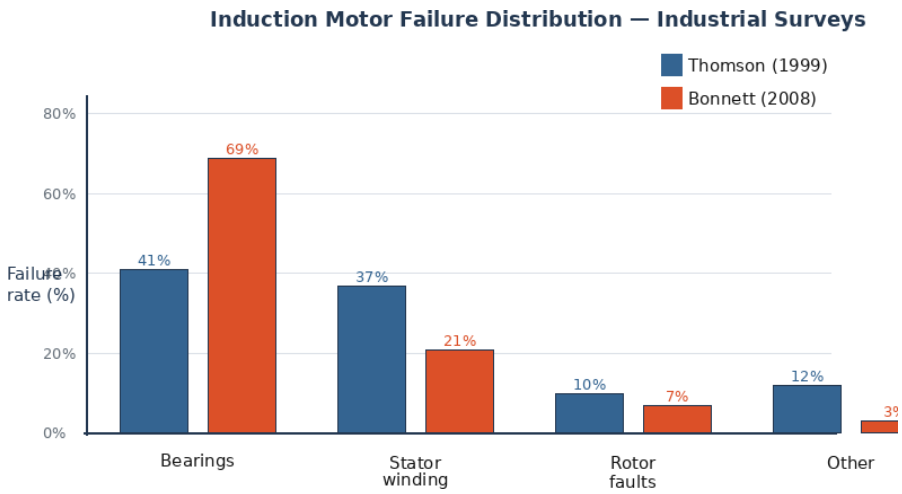


Figure 3 Comparison of induction motor failure distributions

The data reveal a consistent pattern: bearing failures account for the largest share in both surveys (41% in 1999, rising to 69% in 2008), followed by stator winding faults (37% declining to 21%) and rotor faults (10% declining to 7%). The reduction in electrical fault rates reflects advances in insulation materials and winding impregnation techniques, as well as the wider adoption of soft-starters that limit the thermal stress of starting currents. The growth in bearing fault share is partly attributed to the proliferation of voltage-source inverter drives, which generate shaft voltages through capacitive coupling between the rotor and the grounded frame; these shaft voltages drive bearing currents that cause electro-erosive damage to raceways a failure mechanism not present in direct-on-line machines [5].

I.3.2 Stator Winding Faults

Stator failures originate predominantly from the degradation of the winding insulation system, which is simultaneously exposed to the highest electrical, thermal, and mechanical stresses of any machine component.

I.3.2.1 Insulation Degradation Mechanisms

Every insulating material has a rated thermal class specifying the maximum sustained temperature at which it delivers acceptable service life. The Arrhenius model of polymer degradation predicts that the time to failure halves approximately for every 10 °C increase in operating temperature above the rated class a relationship known in engineering practice as the ‘ten-degree rule’. Four distinct stress mechanisms act simultaneously to degrade winding insulation:

Thermal ageing: sustained operation above the rated thermal class accelerates irreversible chemical degradation of the polymer chain structure.

Electrical stress: power-electronic converters generate high dv/dt switching transients (up to several kV/μs) that excite partial discharges at microscopic voids or contaminants within the insulation, progressively eroding the dielectric material.

Mechanical stress: winding vibration driven by electromagnetic forces causes repeated flexing of the conductors, abrading the turn insulation against the slot walls.

Environmental attack: moisture reduces insulation resistance, oil contaminates the dielectric, and chemical agents initiate degradation reactions that would not otherwise occur at operating temperatures.

In practice, these mechanisms are synergistic: thermal softening weakens the insulation mechanically, partial discharges accelerate thermal degradation, and the resulting physical damage provides pathways for moisture ingress. The cumulative effect is insulation degradation that proceeds far more rapidly than any single mechanism would predict [8].

I.3.2.2 Inter-Turn Short Circuit

An inter-turn short circuit the most common and diagnostically most important stator fault occurs when the insulation between two adjacent turns within the same coil is locally breached, creating a low-resistance bypass path for the winding current. Figure I.4 illustrates the coil cross-section with the fault current loop identified [4].

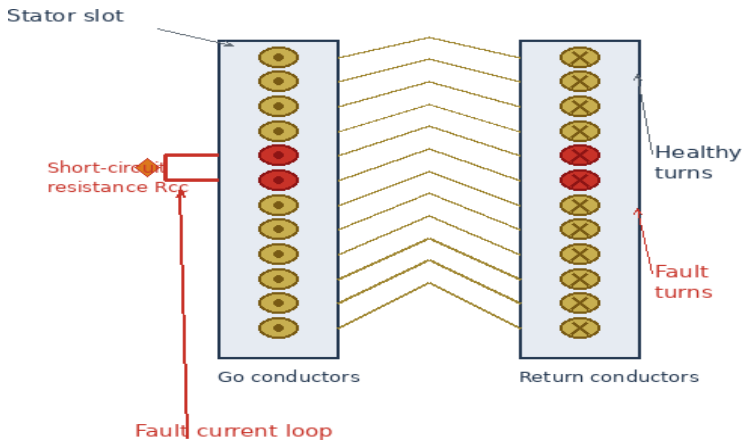


Figure 4 Inter-turn short-circuit fault

The fault current circulating in the shorted loop can be many times larger than the normal phase current because the loop resistance is very small. The resulting Joule heating is concentrated in a small volume of winding, raising local temperatures that rapidly degrade the insulation of adjacent turns. If the fault is not detected and the machine removed from service, the damaged zone expands to involve additional turns, eventually escalating to a coil-to-coil or phase-to-phase fault that destroys the entire winding.

The diagnostic signature of an inter-turn short circuit includes: an asymmetric increase in the amplitude of the affected phase current; torque oscillations at twice the supply frequency; and the emergence of a spectral component near 150 Hz (in a 50 Hz system) attributable to the asymmetric MMF produced by the unbalanced coil [5].

I.3.2.3 Phase-to-Phase and Phase-to-Ground Faults

A phase-to-phase fault involves the failure of the insulation between conductors belonging to two different stator phases. Its severity depends strongly on location within the winding: a fault near the supply terminals drives catastrophic overcurrents that activate protective relays within milliseconds, while a fault near the winding neutral may produce only a modest current asymmetry that is easily overlooked by conventional protection. A phase-to-ground fault in which a winding conductor contacts the grounded machine frame introduces a zero-sequence current path, generates pulsating electromagnetic torque, and represents a shock hazard to personnel. Both types of fault are highly destructive and require immediate machine shutdown [4].

I.3.3 Rotor Faults

Rotor defects create an electromagnetic asymmetry in the cage that modulates the stator currents and torque at frequencies directly related to the slip frequency. These modulation sidebands are the primary signature exploited by spectral diagnostic methods for rotor fault detection.

I.3.3.1 Broken Rotor Bars

Bar fractures are among the most studied rotor defects. A bar may crack at its mid-length or at the bar-to-end-ring junction, most commonly as a result of thermal fatigue from repeated high-current starts, centrifugal stress at high rotational speed, or electromagnetic vibration at slot-harmonic frequencies. When a bar fractures, the current it would normally carry is redistributed to adjacent bars, which become thermally overloaded; in severe cases this cascades into a sequence of secondary bar failures. Figure 5 illustrates the current redistribution pattern associated with a single broken bar.

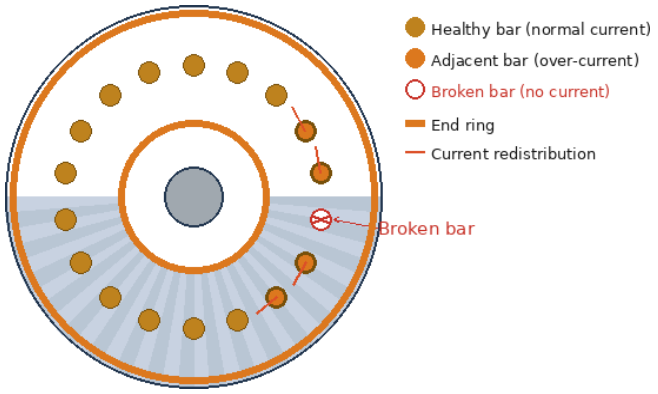


Figure 5 Rotor cage cross-section showing a broken bar

The asymmetric rotor current distribution creates a pulsating field component that, viewed from the stationary stator, appears at the characteristic broken-bar sideband frequencies:

$$f_{brb} = f_s \cdot (1 \pm 2ks), \quad k = 1, 2, 3, \ldots \tag{I.3}$$

where fs is the supply fundamental frequency and s is the slip. Detection of the lower sideband fs(1 − 2s) is the standard Motor Current Signature Analysis indicator for rotor bar fault diagnosis [2].

I.3.3.2 End-Ring Cracks

Cracks propagating through the end rings produce electrical effects indistinguishable from those of broken bars: the interrupted cage current path creates the same asymmetric MMF and the same sideband frequencies described by Equation

I.3. End-ring defects are caused by casting porosity that provides pre-existing crack initiation sites, differential thermal expansion between bar and ring materials under start-stop cycling,

and mechanical overloads that exceed the fatigue strength of the ring material[4].

I.3.3.3 Rotor Eccentricity

Rotor eccentricity is the condition in which the geometric center of the rotor does not coincide with the center of the stator bore, creating a spatially non-uniform air gap. Three distinct forms are recognized in the literature, illustrated in Figure I.6:

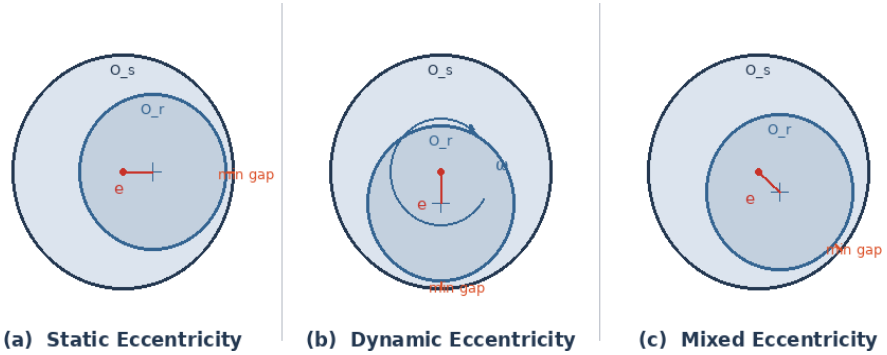


Figure 6 Three types of rotor eccentricity

Static eccentricity: the rotor rotation axis is displaced from the stator bore center but rotation remains centered on the rotor's own axis. The minimum air-gap position is fixed in space.

Dynamic eccentricity: the rotor geometric center is offset from, and orbits around, the stator bore center. The minimum air-gap position sweeps the stator circumference at rotor speed.

Mixed eccentricity: the most common practical case, combining static and dynamic displacement simultaneously.

Eccentricity produces additional spectral components in the stator current at

$$fecc = fs\left[\frac{(kR \pm nd)(1-s)}{p} \pm v\right],\ k = 1,2,\ldots \quad \text{(I.4)}$$

where R is the rotor slot count, nd is the eccentricity order, p is the pole-pair count, and v = 1, 3, 5, … is the stator harmonic order. Beyond the current-spectrum signature, severe eccentricity produces unbalanced magnetic pull a net radial force that overloads the bearings and can ultimately lead to rotor-stator contact [7].

I.3.4 Bearing Faults

Rolling-element bearings are statistically the most failure-prone component in induction

motors. The failure mechanism is typically surface fatigue: cyclic Hertzian contact stresses under rolling-element loads eventually initiate sub-surface cracks that propagate to produce spalls on the raceway or rolling-element surfaces. Each spall generates an impulsive mechanical force when a rolling element traverses it, exciting vibration at the four characteristic bearing defect frequencies:

- BPFO (Ball Pass Frequency, Outer race): generated each time a rolling element passes over a spall on the fixed outer race.
- BPFI (Ball Pass Frequency, Inner race): generated each time a rolling element passes over a spall on the rotating inner race.
- BSF (Ball Spin Frequency): generated by a defect on the surface of a rolling element contacting a race.
- FTF (Fundamental Train Frequency): related to the orbital speed of the rolling-element cage.

These vibration forces perturb the air-gap permanence and thereby introduce corresponding frequency components into the stator current, making both vibration analysis and MCSA applicable to bearing fault detection. The principal causes of bearing degradation include lubricant starvation or contamination, moisture corrosion, shaft-voltage induced electro-erosion in inverter-fed drives, and mechanical damage during assembly [5].

I.3.5 Environmental and External Stresses

External conditions accelerate the degradation of all machine components. High ambient temperature compresses the available thermal margin, forcing the machine to operate closer to its insulation class limit. Humidity reduces insulation resistance and promotes corrosion on metallic surfaces and in bearing lubricants. Airborne dust, chemical vapors, and oil mist can penetrate the machine frame, contaminating the winding insulation and bearing lubricant.

Voltage unbalance at the supply terminals is a particularly damaging and frequently underestimated external stressor. A negative-sequence voltage unbalance of only 2% generates negative-sequence stator currents that may be ten to twenty times larger because the machine presents a low negative-sequence impedance near zero speed producing substantial additional losses in the stator and rotor and increasing the bearing forces. Frequent motor starts impose intense thermal cycling: the starting current of five to seven times the rated value causes rapid Joule heating in both windings and rotor cage, and each start is thermally equivalent from an insulation- ageing perspective to several hours of continuous rated operation [5].

I.4 Diagnostic Methods for Induction Machines

The objective of a condition monitoring system is to extract, from signals measured during normal machine operation, the information required to characterize the machine's health state, identify the fault type and location, and estimate fault severity all without service interruption. The research community has organized the resulting large body of diagnostic technique into three principal families: signal-based methods, model-based methods, and artificial-intelligence methods.

I.4.1 Signal-Based Methods

Signal-based techniques extract diagnostic information directly from measured physical quantities principally stator currents and mechanical vibration without invoking an explicit mathematical model of the machine. Their primary practical advantage is that most of the required sensors are already present in standard motor control centers, making deployment straightforward and cost-effective.

I.4.1.1 Motor Current Signature Analysis (MCSA)

Motor Current Signature Analysis is the most mature and widely deployed on-line diagnostic technique for induction motors. Its operating principle is direct: any electromagnetic asymmetry in the machine, whether caused by a stator fault, a rotor defect, or air-gap irregularity, impresses characteristic frequency components on the stator line current that are absent under healthy conditions. By measuring the stator current with a standard current transformer, computing its frequency spectrum with the Fast Fourier Transform, and comparing the amplitudes at analytically predicted fault frequencies with established threshold values, the presence and approximate severity of a fault can be determined. Figure I.7 illustrates the MCSA signal chain from sensor to decision.

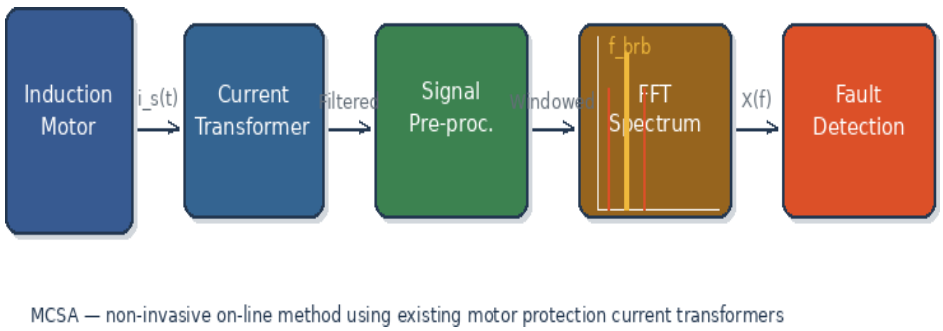


Figure 7 Motor Current Signature Analysis (MCSA)

The principal advantages of MCSA are its complete non-invasiveness the existing motor protection current transformers serve as sensors the ability to monitor the machine without any interruption to operation, and the availability of well-established analytical expressions for the fault frequencies of all major fault types. Its limitations include sensitivity to load variation (which shifts slip-dependent sideband frequencies), masking of low-amplitude sidebands by supply-frequency harmonics and electrical noise, and degraded performance during non-stationary operation such as start-up or load steps. Advanced spectral estimators including MUSIC, ESPRIT, the Short-Time Fourier Transform, and the Wigner-Ville Distribution extend MCSA capability to variable-speed and transient operating conditions [2].

I.4.1.2 Vibration Monitoring

Vibration analysis is the classical technique for detecting mechanical defects, and its application to bearing fault detection in particular has the longest industrial track record. Piezoelectric accelerometers mounted on the bearing housings measure vibration acceleration in radial, axial, and tangential directions. Figure I.8 illustrates the measurement setup with accelerometers positioned on the bearing housing and connected to a data acquisition unit.

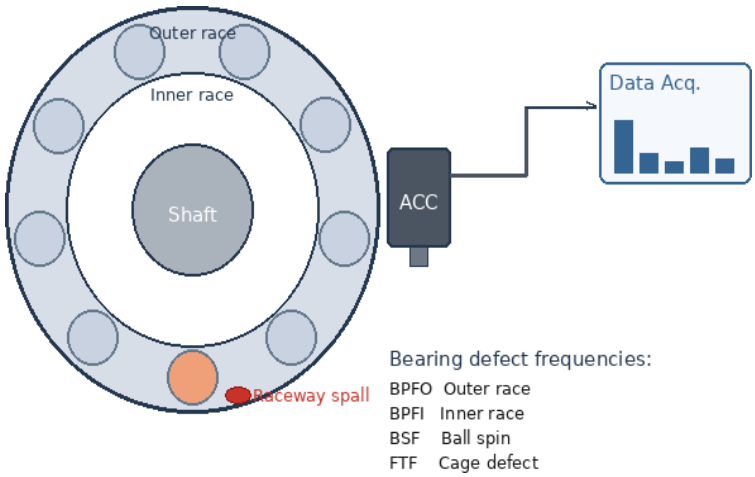


Figure 8 Bearing condition monitoring and characteristic defect frequencies.

The vibration spectrum is examined for the four characteristic bearing defect frequencies. Envelope analysis demodulation of the high-frequency vibration signal band-passed around a structural resonance, followed by FFT of the envelope is particularly effective at detecting incipient bearing defects whose force impulses are too small to produce visible spectral peaks in the raw vibration spectrum. Statistical time-domain indicators RMS, kurtosis, crest factor, and shape factor complement spectral analysis by providing scalar summary measures of

overall vibration severity that can be monitored for upward trends [10].

I.4.1.3 The Park Vector Approach

The Park vector method transforms the three-phase stator currents into two orthogonal components in the rotating reference frame. Under healthy, balanced, sinusoidal conditions, the locus of the instantaneous current space vector traces a perfect circle. Any electromagnetic asymmetry inter-turn fault, broken bar, supply unbalance, eccentricity distorts this circle into an ellipse or a more complex shape. The diagnostic indicators derived from the locus include the ellipse eccentricity, the amplitude of harmonic components of the vector modulus, and pixel-density maps that can be processed by pattern recognition algorithms. The method provides an intuitive visual representation of machine health without requiring detailed spectral analysis expertise, though its sensitivity decreases at light loads [10].

I.4.1.4 Thermal and Stray-Flux Monitoring

Thermographic inspection with an infrared camera maps the temperature distribution of the machine frame, connection box, and accessible winding surfaces without physical contact. Hot spots associated with localized Joule heating in damaged winding sections, elevated iron losses near lamination defects, or overloaded bearings are identifiable by comparison with a reference image taken under identical conditions on a healthy machine. Stray axial flux monitoring employs a search coil placed outside the machine frame, oriented perpendicular to the rotor axis; the axial flux component, negligible in a symmetric machine, grows with any rotor or stator asymmetry and exhibits the same fault-frequency signatures as the stator current, sometimes with reduced interference from supply harmonics at light load [9].

I.4.2 Model-Based Diagnostic Methods

Model-based techniques compare the observed machine behavior with that predicted by a mathematical model of the healthy machine. The difference the residual is monitored for fault-induced deviations that exceed a statistical threshold. Three principal model structures are employed in the induction machine diagnostic literature:

- State observers (Luenberger observer, Extended Kalman Filter): the observer reconstructs the full machine state vector from measured stator voltages and currents. A fault modifies the actual system dynamics; the resulting growth in the observer residual reveals both the presence and the nature of the defect.
- Parametric identification: the parameters of an equivalent-circuit model stator resistance, rotor resistance, leakage inductance, magnetizing inductance are estimated continuously from measured data. A statistically significant shift in a fitted parameter signals a specific fault: an increase in rotor resistance is consistent with bar breakage, a reduction in stator inductance is consistent with an inter-turn short circuit.
- Parity equations (analytical redundancy): algebraic or differential relationships between measured quantities that must hold exactly under healthy conditions are formulated; persistent violation of a parity equation signals a defect in the corresponding machine subsystem.

The Park equivalent-circuit model of the machine in the rotor-fixed reference frame is the most common foundation for model-based diagnosis:

$$U_{dqs} = Rs \cdot idqs + \frac{d(phi\ dqs)}{dt} + omega \cdot J \cdot phi\ dqs \quad \text{(I.5)}$$

$$0 = Rr \cdot Idqr + \frac{d(phi_{dqr})}{dt} \quad \text{(I.6)}$$

$$phi_{dqs} = Lf \cdot idqs + Lm \cdot (idqs + idqr) \quad \text{(I.7)}$$

$$phi_{dqr} = Lm \cdot (idqs + idqr) \quad \text{(I.8)}$$

In the healthy machine the parameter set {*Rs, Rr, Lf, Lm*} is constant. A stator inter-turn fault introduces an additional current source proportional to the short- circuit ratio μcc into Equation I.5; a broken rotor bar introduces an asymmetric resistance matrix *Rdef* into Equation I.6. Parametric identification methods estimate these extended parameter sets and compare them against reference values to produce quantitative fault indicators [3].

The strength of model-based methods lies in their theoretical sensitivity and their ability to separate fault-induced parameter changes from normal variation caused by temperature or magnetic saturation. Their practical limitation is the requirement for an accurately identified machine model, which is difficult to obtain for a motor already installed in service without prior commissioning tests [7].

I.4.3 Artificial Intelligence-Based Methods

The nonlinear dynamics of induction machines and the high variability of industrial operating conditions motivate data-driven AI classifiers that learn fault signatures directly from measurements, without requiring derivation of an explicit physical model. Three AI approaches have been most extensively studied for induction machine diagnosis [6].

I.4.3.1 Artificial Neural Networks

Multi-layer feedforward neural networks learn a nonlinear mapping from a feature input vector composed of spectral amplitudes, statistical indicators, or wavelet coefficients extracted from measured signals to fault class output labels. Once trained on a labeled dataset by the backpropagation algorithm, the trained network classifies new measurements in real time at negligible computational cost. The main limitation is the 'black-box' character of the learned representation: the weight values carry no physical interpretation, making it difficult to validate or explain the diagnostic decisions a concern in safety-critical applications [6].

I.4.3.2 Fuzzy Logic Systems

Fuzzy logic represents diagnostic knowledge as a set of interpretable IF-THEN rules using linguistic variables. A rule such as 'IF the broken-bar sideband amplitude relative to the fundamental is HIGH AND the slip is MEDIUM THEN the rotor bar fault severity is SIGNIFICANT' is both physically motivated and transparent to a maintenance technician. Gradual membership-function transitions provide inherent robustness to measurement noise, and the rule base can incorporate expert knowledge accumulated over years of field experience. The main limitation is the difficulty of specifying effective membership functions and rules when labeled fault data are scarce [8].

I.4.3.3 Adaptive Neuro-Fuzzy Inference Systems (ANFIS)

ANFIS, the approach adopted in this thesis, is a hybrid architecture that integrates the interpretability of a Takagi-Sugeno fuzzy inference system with the adaptive learning capability of a neural network [11].

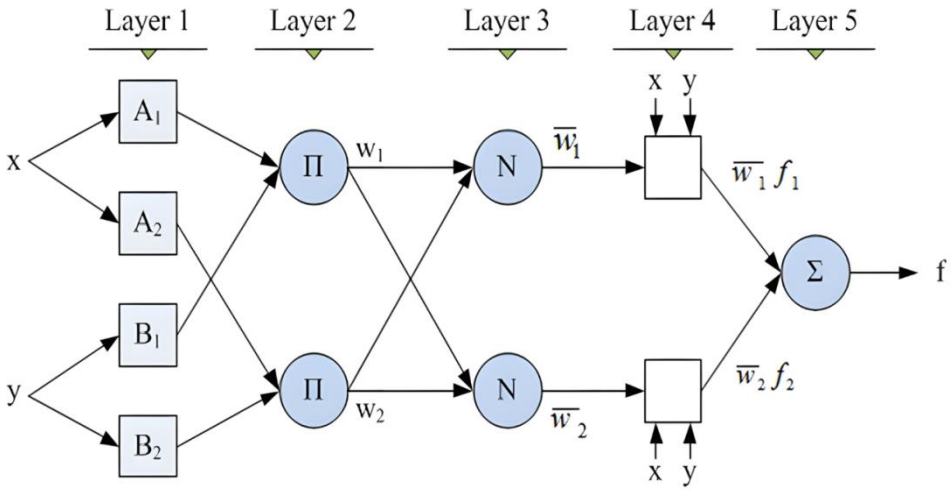


Figure 9 Five-layer ANFIS architecture and functional layers tuned by hybrid training

The network parameters membership function shapes (antecedents) and rule consequent coefficients are tuned automatically from training data by a hybrid algorithm that alternates between least-squares estimation for the consequent parameters and gradient-descent backpropagation for the antecedent parameters. This hybrid approach converges significantly faster than pure gradient descent and typically requires less labeled data than a stand-alone neural network of comparable accuracy.

The resulting system retains the linguistically interpretable rule structure of a fuzzy inference system while achieving the classification accuracy of a data-driven neural network. Published comparative studies consistently show that ANFIS achieves higher accuracy than both stand-alone neural networks and manually designed fuzzy rule bases for multi-class induction machine fault diagnosis, particularly when the boundary between fault classes is gradual rather than abrupt as is the case for intermediate severity levels of inter-turn and bar-breakage faults [6].

Table 2 Comparative summary of the three main diagnostic method families

Family	Core principle	Key advantages	Principal limitations
Signal-based (MCSA, vibration, Park vector)	Spectral or statistical analysis of measured physical signals	Non-invasive; uses existing sensors; real- time; analytically grounded fault-frequency indices	Sensitive to load variation; sidebands masked by harmonics; limited under non- stationary conditions
Model-based (observers, parametric ID)	Residuals between model predictions and actual machine measurements	High theoretical sensitivity; fault localization; separates fault from normal parameter variation	Requires accurate, well-identified machine model; computationally intensive
AI-based (ANN, Fuzzy, ANFIS)	Data-driven learning of fault classification from labelled training data	Handles strong nonlinearity; high accuracy; no explicit model required; robust to noise	Requires labeled training data; ANN lacks interpretability; overfitting risk with small datasets

Table 3 Attribute comparison of principal AI diagnostic methods for induction machines

Method	Classification accuracy	Result interpretability	Training data volume needed	Real-time computational cost
Multi-layer ANN (MLP)	High (90–99%)	Low — black box	Large (100 + per class)	Low (fast inference)
Radial Basis Function Net	High	Low	Moderate	Very low
Support Vector Machine (SVM)	Very high	Medium	Moderate	Low
Fuzzy Logic (expert	Medium to	Very high —	Small (expert	Very low

rules)	high	Interpretable	knowledge)	
ANFIS (neuro-fuzzy)	High to very high	High — linguistic rules	Moderate	Low
Convolutional Neural Net	Very high	Very low	Very large	High (GPU required)
Random Forest	High	High — tree structure	Moderate	Very low

I.5 Conclusion

In this chapter, we reviewed the structural composition of the induction machine, detailing its various components such as the stator, rotor, windings, rotor bars, and bearings. Next, we presented a classification of induction machine faults, distinguishing between stator, rotor, and mechanical failures. For each fault type, we described the symptoms that may manifest and their potential consequences on the machine's operation. Finally, we provided a non-exhaustive overview of the different fault diagnosis methods for induction machines, briefly explaining the operation of each approach while highlighting its respective advantages and limitations.

CHAPTER II

Modeling of the squirrel-cage asynchronous machine

II.1 Introduction

In this chapter, we focus on the mathematical modeling of the squirrel-cage induction machine. The goal is to build a model that accurately reflects the real behavior of the machine, both under normal operating conditions and in the presence of a fault.

To do so, we start by establishing the healthy operation model, using the Park transformation. This transformation allows us to work in a rotating two-phase reference frame, which makes the equations much easier to handle and solve. The simulation results obtained from this model will then be presented in order to verify that it behaves as expected.

In a second step, we extend this model to incorporate the inter-turn short-circuit fault at the stator. This type of fault alters the electromagnetic interactions within the machine, and it is therefore necessary to account for it in the equations. The simulations carried out with this faulty model will allow us to concretely observe the impact of the fault on the electrical and mechanical quantities of the machine.

II.2 Mathematical Model of the Healthy Machine

II.2.1 Electrical Equations of the Induction Motor

The induction machine is based on the electromagnetic coupling of two distinct circuits: the stator and the rotor. Modeling the machine in a three-phase reference frame requires establishing a system of differential equations governing the interactions between voltages, currents, and fluxes for all windings [11].

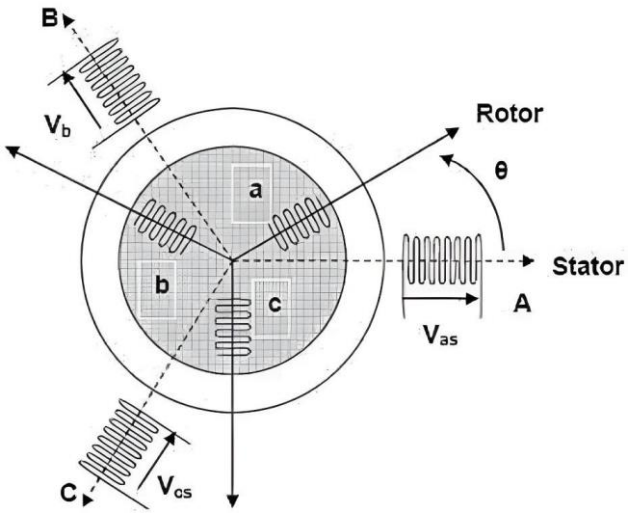


Figure 10 Schematic representation of a three-phase induction machine.

The voltage equations governing the operation of an asynchronous machine are expressed in matrix form [11]:

$$\begin{cases} u_s = [R_s].i_s + \dfrac{d}{dt}\phi_s \\ 0 = [R_r].i_r + \dfrac{d}{dt}\phi_r \end{cases} \tag{II.1}$$

$$u_s = \begin{bmatrix} u_{sa} \\ u_{sb} \\ u_{sc} \end{bmatrix}; \quad i_s = \begin{bmatrix} i_{sa} \\ i_{sb} \\ i_{sc} \end{bmatrix}; \quad \phi_s = \begin{bmatrix} \phi_{sa} \\ \phi_{sb} \\ \phi_{sc} \end{bmatrix}; \quad [R_s] = \begin{bmatrix} R_s & 0 & 0 \\ 0 & R_s & 0 \\ 0 & 0 & R_s \end{bmatrix}$$

$$u_r = \begin{bmatrix} u_{ra} \\ u_{rb} \\ u_{rc} \end{bmatrix}; \quad i_r = \begin{bmatrix} i_{ra} \\ i_{rb} \\ i_{rc} \end{bmatrix}; \quad \phi_r = \begin{bmatrix} \phi_{ra} \\ \phi_{rb} \\ \phi_{rc} \end{bmatrix}; \quad [R_r] = \begin{bmatrix} R_r & 0 & 0 \\ 0 & R_r & 0 \\ 0 & 0 & R_r \end{bmatrix}$$

where :

$\boldsymbol{U_s}$, $\boldsymbol{U_r}$**:** Stator and rotor voltage vectors.

$\boldsymbol{i_s}$, $\boldsymbol{i_r}$**:** Stator and rotor current vectors.

$\boldsymbol{\Phi_s}$, $\boldsymbol{\Phi_r}$**:** Stator and rotor flux linkage vectors.

$[\boldsymbol{R_s}]$, $[\boldsymbol{R_r}]$**:** Stator and rotor resistance matrices.

The total flux linkages and $\boldsymbol{\Phi_r}$ of the stator and rotor phases are expressed as follows:

$$\begin{cases} \phi_s = [L_s].i_s + [M_{rs}].i_r \\ \phi_r = [M_{rs}].i_s + [L_r].i_r \end{cases} \quad \text{(II.2)}$$

Due to the machine's isotropy and symmetry, the self-inductances of the stator phases are equal, as are those of the rotor. Thus, the matrices [Ls] and [Lr] become:

$$[L_s] = \begin{bmatrix} L_{sp} & M_s & M_s \\ M_s & L_{sp} & M_s \\ M_s & M_s & L_{sp} \end{bmatrix} \quad \text{(II.3)}$$

$$[L_r] = \begin{bmatrix} L_{rp} & M_r & M_r \\ M_r & L_{rp} & M_r \\ M_r & M_r & L_{rp} \end{bmatrix} \quad \text{(II.4)}$$

where :

***L_{sp}, L_{rp}*:** Stator and rotor self-inductances.

Ms: Mutual inductance between two stator phases.

Mr : Mutual inductance between two rotor phases.

The mutual inductance matrix between the stator and rotor phases depends on the angular position θ (theta) between the stator and rotor axes:

$$[\mathrm{M_{rs}}] = [\mathrm{M_{sr}}]^{\mathrm{T}} = \mathrm{M_{rs}} \begin{bmatrix} \cos(p\theta) & \cos(p\theta - 2\pi/3) & \cos(p\theta - 4\pi/3) \\ \cos(p\theta - 4\pi/3) & \cos(p\theta) & \cos(p\theta - 2\pi/3) \\ \cos(p\theta - 2\pi/3) & \cos(p\theta - 4\pi/3) & \cos(p\theta) \end{bmatrix} \quad \text{(II.5)}$$

The induction motor model presented above is relatively complex because the inductance matrix contains elements that vary with the rotation angle θ (theta). To simplify this model, mathematical transformations are applied to the system.

A common approach for studying rotating machines involves changing the three-phase (abc) reference frame to a two-phase (dq) frame. This is known as the Park transformation. In addition to its simplicity, the Park model significantly reduces both computational overhead and simulation time [11].

II.2.2 The Park Transformation and the dq Model

II.2.2.1 Principle of the Park Transformation

The Park transformation maps the three-phase (abc) quantities to an equivalent two- phase (dq0) reference frame rotating at an angular speed ωs, which can be chosen freely (ωs = 0 for the stationary frame, ωs = ωe for the synchronous frame, ωs = ωr for the rotor frame) [13].

The transformation matrix [P(θs)] is:

$$[p(\theta_s)] = \frac{2}{3}.\begin{vmatrix} \cos(\theta_s) & \cos(\theta_s) & \cos(\theta_s) \\ -\sin(\theta_s) & -\sin(\theta_s) & -sin(\theta_s) \\ \frac{1}{2} & \frac{1}{2} & \frac{1}{2} \end{vmatrix} \quad \text{(II.6)}$$

where $\theta = \omega s \cdot t$ is the angle of the rotating frame with respect to the phase-a axis, and the factor (2/3) corresponds to the amplitude-invariant normalization convention adopted here, consistent.

The inverse transformation $P^{-1}(\theta)$ is given by:

$$P^{-1}(\theta) = \begin{bmatrix} \cos(\theta) & -\sin(\theta) & 1 \\ \cos\left(\theta - \frac{2\pi}{3}\right) & -\sin\left(\theta - \frac{2\pi}{3}\right) & 1 \\ \cos\left(\theta + \frac{2\pi}{3}\right) & -\sin\left(\theta + \frac{2\pi}{3}\right) & 1 \end{bmatrix} \quad \text{(II.7)}$$

II.2.2.2 Voltage Equations in the dq Reference Frame

After applying the Park transformation with a synchronously rotating frame (ωs = ωe), the stator voltage equations become:

$$Vds = Rs \cdot ids + \frac{d\varphi ds}{dt} - \omega e \cdot \varphi qs \quad \text{(II.8)}$$

$$Vqs = Rs \cdot iqs + \frac{d\varphi qs}{dt} + \omega e \cdot \varphi ds \quad \text{(II.9)}$$

and the rotor voltage equations (short-circuited rotor, Vdr = Vqr = 0):

$$0 = Rr \cdot idr + \frac{d\varphi dr}{dt} - (\omega e - \omega r) \cdot \varphi qr \quad \text{(II.10)}$$

$$0 = Rr \cdot iqr + \frac{d\varphi qr}{dt} + (\omega e - \omega r) \cdot \varphi dr \quad \text{(II.11)}$$

where ωr = P·Ω is the electrical rotor speed, Ω is the mechanical rotor speed in rad/s, and (ωe − ωr) = s·ωe is the slip angular frequency [12-13].

II.2.2.3 Flux Linkage Equations in the dq Frame

The flux linkage equations in the dq frame take the compact form:

$$\varphi ds = Ls \cdot ids + Lm \cdot idr \quad \text{(II.12)}$$

$$\varphi qs = Ls \cdot iqs + Lm \cdot iqr \quad \text{(II.13)}$$

$$\varphi dr = Lr \cdot idr + Lm \cdot ids \quad \text{(II.14)}$$

$$\varphi qr = Lr \cdot iqr + Lm \cdot iqs \quad \text{(II.15)}$$

where Ls = lfs + Lm, Lr = lfr + Lm, and Lm is the magnetizing inductance (equivalent to (3/2)·Msr). These equations confirm that [Msr] no longer appears in its trigonometric form the transformation has completely decoupled the angular dependence [13-14].

II.2.2.4 State-Space Formulation

Equations (II.8) and (II.15) can be combined into a state-space system with state vector X = [ids, iqs, idr, iqr]^T and input vector U = [Vds, Vqs, 0, 0]^T. After substituting the flux equations into the voltage equations and solving for the current derivatives, the state equations are:

$$\frac{d(ids)}{dt} = \left(\frac{1}{\sigma Ls}\right) \cdot \left[Vds - Rs \cdot ids + \left(\frac{Lm}{Lr}\right) \cdot (Rr \cdot idr + (\omega e - \omega r) \cdot Lr \cdot iqr) + \omega \cdot \sigma Ls \cdot iqs\right] \quad \text{(II.16)}$$

$$\frac{d(iqs)}{dt} = \left(\frac{1}{\sigma Ls}\right) \cdot \left[Vqs - Rs \cdot iqs + \left(\frac{Lm}{Lr}\right) \cdot (Rr \cdot iqr - (\omega e - \omega r) \cdot Lr \cdot idr) - \omega e \cdot \sigma Ls \cdot ids\right] \quad \text{(II.17)}$$

$$\frac{d(idr)}{dt} = \left(\frac{Lm}{\sigma LsLr}\right) \cdot [Rs \cdot ids - Vds] + \left(-\frac{Rr}{\sigma Lr}\right) \cdot idr + (\omega e - \omega r) \cdot iqr - \left(\omega e \cdot \frac{Lm}{\sigma Lr \cdot Ls}\right) \cdot iqs] \quad \text{(II.18)}$$

$$\frac{d(iqr)}{dt} = \left(\frac{Lm}{\sigma LsLr}\right) \cdot [Rs \cdot iqs - Vqs] + \left(-\frac{Rr}{\sigma Lr}\right) \cdot iqr - (\omega e - \omega r) \cdot idr + \omega e \cdot \frac{Lm}{\sigma Lr \cdot Ls} \cdot ids] \quad \text{(II.19)}$$

where σ = 1 − Lm²/(Ls·Lr) is the total leakage factor of the machine. This parameter plays central role in the dynamic behaviour: a small σ implies tight magnetic coupling between stator and rotor, which produces a fast torque response [12].

II.3 Mechanical Equation of Motion

The electromagnetic model must be completed by Newton's second law applied to the rotating mass. The mechanical equation relates the net torque acting on the rotor to its angular acceleration:

$$J \cdot \frac{d\Omega}{dt} = Cem - Cr - f \cdot \Omega \quad \text{(II.20)}$$

where J is the total moment of inertia of the rotor and load (kg·m²), Cem is the electromagnetic torque (N·m), Cr is the load resistive torque (N·m), f is the viscous friction coefficient (N·m·s/rad), and Ω is the mechanical rotor speed (rad/s) [13].

The electromagnetic torque is expressed in terms of the dq currents and flux linkages as:

$$Cem = \left(\frac{3}{2}\right) \cdot P \cdot Lm \cdot (iqs \cdot idr - ids \cdot iqr) \quad \text{(II.21)}$$

or equivalently using only flux linkages:

$$Cem = \left(\frac{3}{2}\right) \cdot P \cdot (\varphi ds \cdot iqs - \varphi qs \cdot ids) \quad \text{(II.22)}$$

Both expressions are numerically equivalent under the dq model and produce identical simulation results. Expression (II.21) is adopted here because it is directly computable from the state variables ids, iqs, idr, iqr without additional flux computations [11-12].

The complete machine model therefore consists of the four electrical state equations (II.8) and (II.20) coupled to the mechanical equation (II.20) through the electromagnetic torque (II.21). This five-equation system, implemented as a MATLAB Function block in Simulink, constitutes the simulation model described.

II.4 Modeling of the Stator Inter-Turn Short-Circuit Fault

II.4.1 Physical Description of the Fault

An inter-turn short circuit in the stator winding occurs when the insulation between adjacent turns within the same coil is locally breached, creating a low-resistance bypass path the fault resistance Rcc for part of the winding current. If μcc turns are shorted out of a total of N turns in the affected coil, then a fraction μ = μcc/N of the winding is bypassed [11].

The shorted turns form a closed loop driven by the portion of the phase voltage corresponding to those turns. Because Rcc is typically much smaller than the normal winding impedance, the resulting circulating fault current Icc can be many times larger than the rated phase current, causing intense localized Joule heating that rapidly propagates the damage [5].

From a circuit perspective, the inter-turn fault in phase A introduces an additional current source of magnitude Icc into the stator circuit equations and modifies the effective stator resistance of the affected phase. The healthy three-phase symmetry is therefore broken, and the machine equations in the dq frame must be extended to account for this asymmetry [11].

II.4.2 Modified Voltage Equations with the Fault

Let phase A of the stator winding be the affected phase. If μ = Ncc/N is the short-circuit ratio (0 < μ < 1), the voltage equation of the faulted phase A is modified as follows:

$$Vsa = Rs \cdot Isa - \mu \cdot Rs \cdot Icc + Lfs \cdot \frac{d(Isa)}{dt} - \mu \cdot Lfs \cdot \frac{d(Icc)}{dt} + \frac{d\varphi sa_m}{dt} \quad \text{(II.23)}$$

The equation for the fault current loop itself is:

$$0 = Rcc \cdot Icc + \mu \cdot Rs \cdot Isa - \mu^2 \cdot Rs \cdot Icc + \mu \cdot Lfs \cdot \frac{d(Isa)}{dt} - \mu^2 \cdot Lfs \cdot \frac{d(Icc)}{dt} + \mu \cdot \frac{d\varphi sa_m}{dt} \quad \text{(II.24)}$$

where Rcc is the contact resistance of the short circuit, Isa is the phase A stator current, and φsam is the mutual flux linkage component of phase A. The phases B and C remain healthy and retain their original voltage equations [11].

II.4.3 Effect of the Fault on the dq Model

Applying the Park transformation to the modified three-phase equations yields a dq model that contains additional terms proportional to μ and Icc. These additional terms appear as disturbance inputs to the d- and q-axis voltage equations:

$$Vds_fault = Vds - \mu \cdot (Rs \cdot iccd + Lfs \cdot \frac{d(iccd)}{dt}) \quad \text{(II.25)}$$

$$Vqs_fault = Vqs - \mu \cdot \left(Rs \cdot iccq + Lfs \cdot \frac{d(iccq)}{dt}\right) \quad \text{(II.26)}$$

where iccd and iccq are the d- and q-axis projections of the fault current Icc. In steady- state sinusoidal conditions, these terms introduce a component at twice the supply frequency (2·fe) in the torque and a spectral component near 150 Hz in the stator current spectrum two of the key diagnostic indicators exploited [5, 11].

The electromagnetic torque expression is also modified:

$$Cem_fault = Cem_healthy - \left(\frac{3}{2}\right) \cdot P \cdot \mu \cdot Lm \cdot (iccd \cdot iqr - iccq \cdot idr) \quad \text{(II.27)}$$

This additional term produces the torque oscillations at 2·fe that are characteristic of stator winding asymmetry and constitute one of the primary fault indicators observables in the simulation results [5].

II.5 Simulink Implementation (Healthy Machine)

Figure 11 shows the complete Simulink diagram of the healthy machine model. The three-phase supply voltages Vsa, Vsb, Vsc generated by ideal sinusoidal sources are transformed into Park components (Vds, Vqs) by the "Park" block (green, left). The central "MATLAB Function" block (yellow) implements the state equations (II.8) and (II.20) in MATLAB code; its outputs the derivatives of the flux linkages and rotor speed are integrated by the 1/s blocks. The integrated state variables are fed back to the state computation block, closing the feedback loop characteristic of a dynamical system. The inverse Park transformation block ("parkinv", green, right) recovers the phase currents isa, isb, isc in the natural (a, b, c) frame.

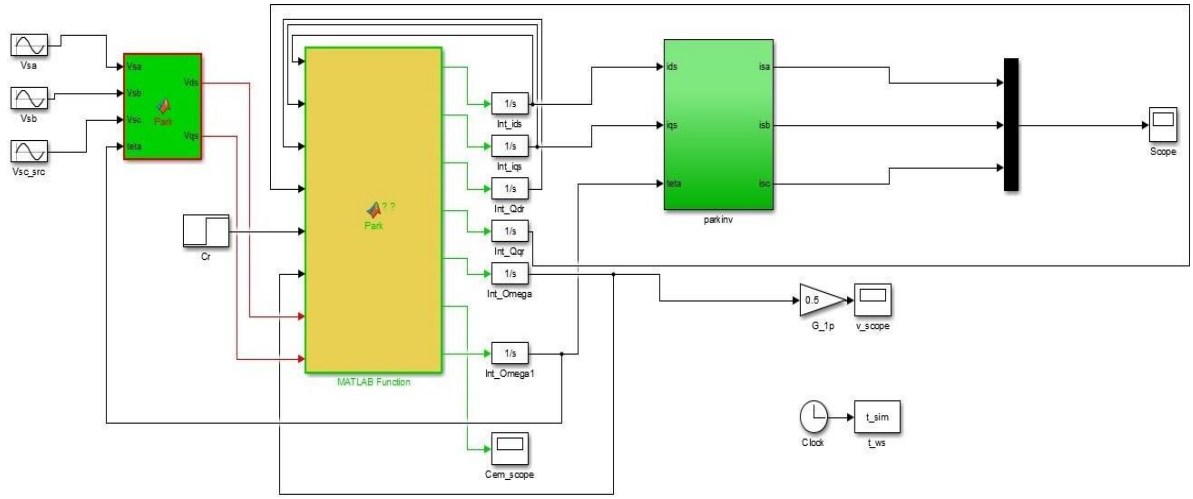


Figure 11 Simulink/MATLAB Modeling of a Squirrel-Cage Induction Motor

The transformation angle θ is provided in real time by the variable tws, computed from the simulator clock. The numerical solver used is the variable-step ODE45 solver (4th/5th-order Runge–Kutta) with a relative tolerance of 1×10^{-6}, which provides sufficient numerical accuracy for the stiff ODEs characteristic of electrical machines while maintaining acceptable computation times for second-scale simulations. The output sampling time step is fixed at 1×10^{-4} s, corresponding to a sampling frequency of 10 kHz well above the Nyquist frequency for all relevant spectral components (< 500 Hz).

II.5.1 Simulation Results for healthy Operation

The healthy-machine simulations are run for a total duration of 2 seconds. The machine starts at no load (Cr = 0 N·m) and a resistive load torque of 5 N·m is applied at t = 1 s to simulate rated-load operation. The results presented below illustrate the expected electromechanical behavior of a healthy, balanced three-phase induction machine.

II.5.2 Stator Currents for healthy Operation

Figure 12 shows the time evolution of the three stator phase currents (isa, isb, isc) over the full simulation duration, with an inset zoom over the interval [1.4–1.45 s] to examine the waveform in steady-state under load. At direct-on-line starting (t = 0 s), the currents exhibit a large inrush peak of approximately ±20 A characteristic of the starting current transient of induction motors, typically 5 to 7 times the rated current before damping to a low-amplitude oscillatory steady state between t ≈ 0.15 s and t = 1 s (no-load operation) [9].

The application of the load torque at t = 1 s causes an increase in current amplitude, from approximately ±1 A (no load) to approximately ±2.8 A (rated load), reflecting the increase in slip and electromagnetic torque. The zoom over [1.4–1.45 s] reveals the perfect three-phase symmetry of the steady-state currents: all three phases exhibit strictly equal amplitudes (≈ 2.8 a peak) and a mutual phase shift of exactly 120°, fully consistent with the expected behavior of a healthy machine supplied by a balanced three-phase voltage system. No spurious harmonic components are observable in this regime.

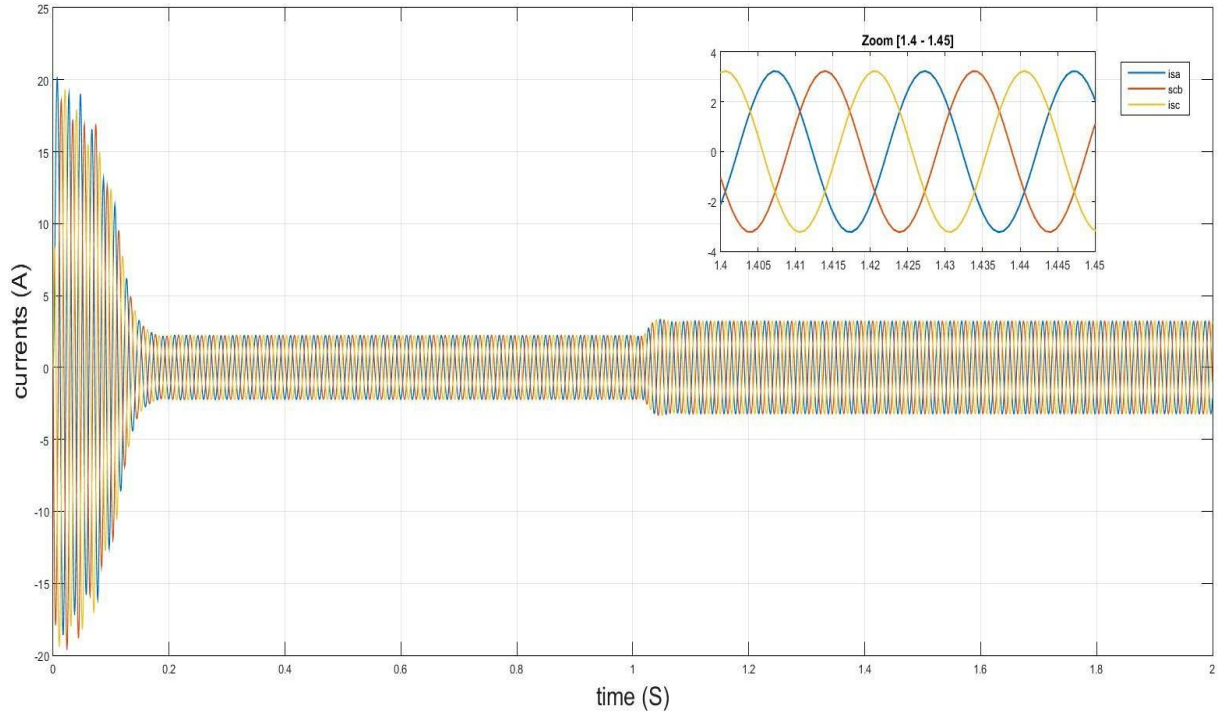


Figure 12 Evolution of Stator Phase Currents During Startup and Under Load Conditions

II.5.3 Electromagnetic Torque for healthy Operation

Figure 14 presents the time evolution of the electromagnetic torque Cem under healthy operation. During starting, the torque exhibits heavily damped oscillations with an initial peak

of approximately 27 N·m before converging to a near-zero value at no load (t ∈ [0.2; 1.0] s). This transient oscillatory behavior is characteristic of direct-on-line starting of induction machines and results from the interaction between the stator and rotor flux components during the establishment of steady-state operation .

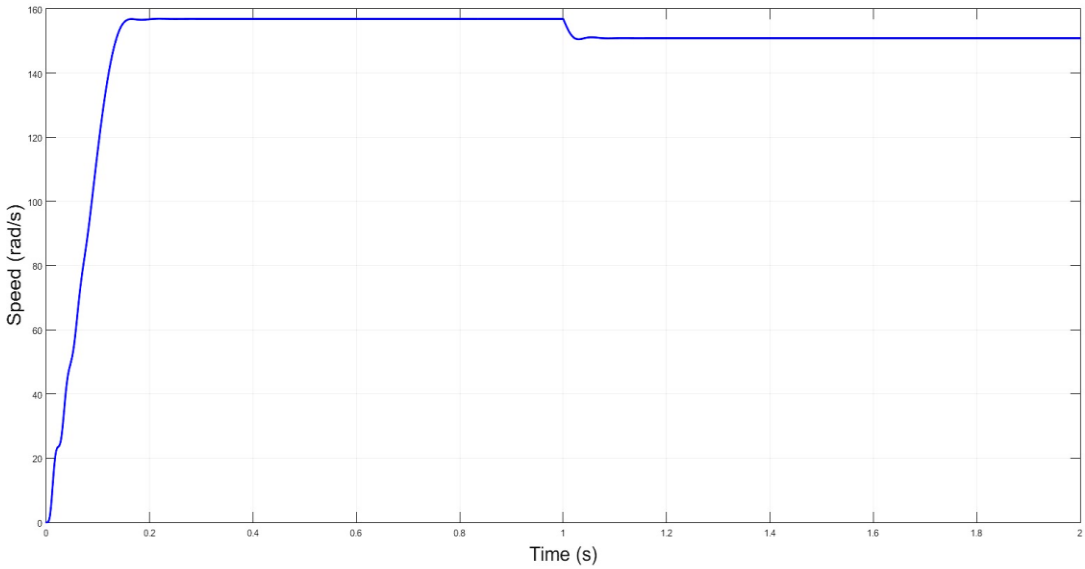


Figure 13 Evolution of Rotational Speed During Startup and Under Load Conditions

After the application of the 5 N·m load torque at t = 1 s, the electromagnetic torque converges rapidly and settles at a steady-state value of approximately 5.2 N·m, compensating the resistive torque and the viscous friction losses described by equation (II.20). The fast settling (within 0.1 s) confirms the good dynamic response of the model. Critically, the steady-state healthy torque is perfectly smooth, with zero ripples this constitutes the key reference against which the faulty case will be compared.

II.5.4 Rotor Speed for healthy Operation

Figure 13 shows the rotor angular speed Ω (rad/s) under healthy operation. The machine accelerates rapidly from rest to near-synchronous speed at no load (Ω ≈ 157 rad/s ≈ 1500 rpm for p = 2 pole pairs at 50 Hz), with a slight initial overshoot characteristic of the transient regime. In steady-state at no load, the speed stabilizes at approximately 157 rad/s, corresponding to a near-zero slip, consistent with the specifications of a well-designed squirrel-cage machine

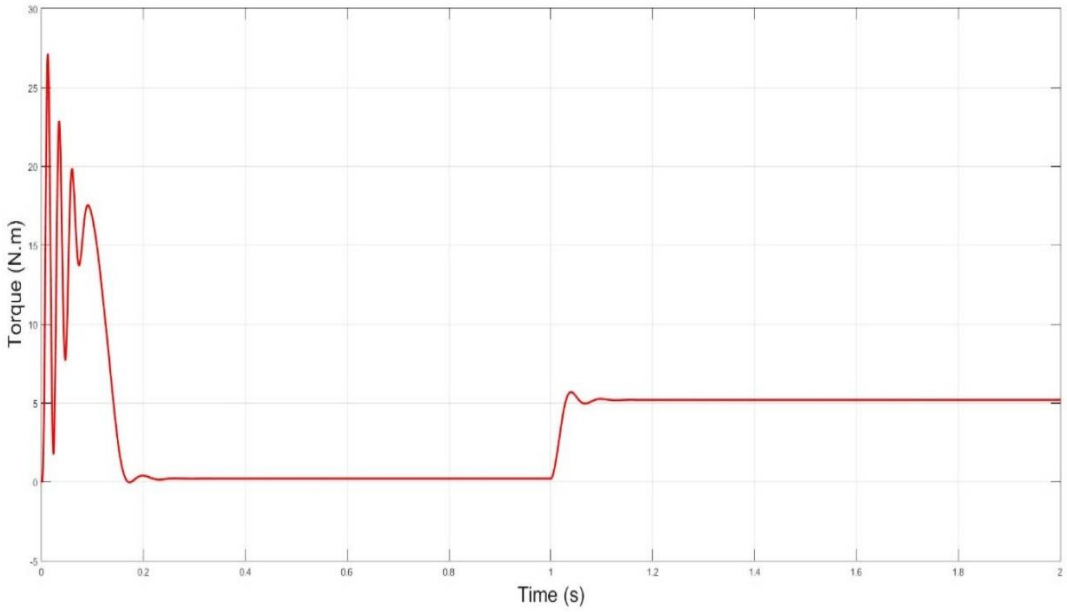


Figure 14 Evolution of Electromagnetic Torque During Startup and Under Load Conditions

The application of the 5 N·m load torque at t = 1 s causes the speed to decrease to $\Omega \approx 151$ rad/s, corresponding to a steady-state slip of $s = (157 - 151)/157 \approx 3.8\%$, which is consistent with the specifications of a 1.5 kW induction machine operating at rated load [17]. The speed transition is smooth and monotone, with no significant oscillation, confirming the stability of the model equilibrium.

II.6 Simulink Implementation (Machine with Stator Fault)

The Simulink model for the faulty case is an extension of the healthy model in which the state computation block is replaced by one that incorporates the modified equations (II.23) and (II.21) and computes the short-circuit current icc via. An additional subsystem, referred to as the short-circuit block, models the short-circuit loop and calculates the resulting perturbation terms eds_cc and eqs_cc as functions of the fault severity μ and the current state variables (Figure 15). The fault severity is parameterized through Step blocks (Step2), allowing the fault to be introduced at a precisely defined instant during the simulation.

Figure 16 presents the complete Simulink diagram of the faulty model. The overall structure is identical to the healthy model, with the addition of the short-circuit block (top, pink block), which receives the Park voltage components, the fault parameters (ncc1, ncc2, ncc3) and produces the short-circuit current ldqccs. This current is added to the state currents computed by the main block (yellow), modifying the stator flux linkages and, consequently, the electromagnetic torque and rotor speed. The inverse transformation block (blue-violet, right) delivers the measurable phase currents isa, isb, isc in the natural frame.

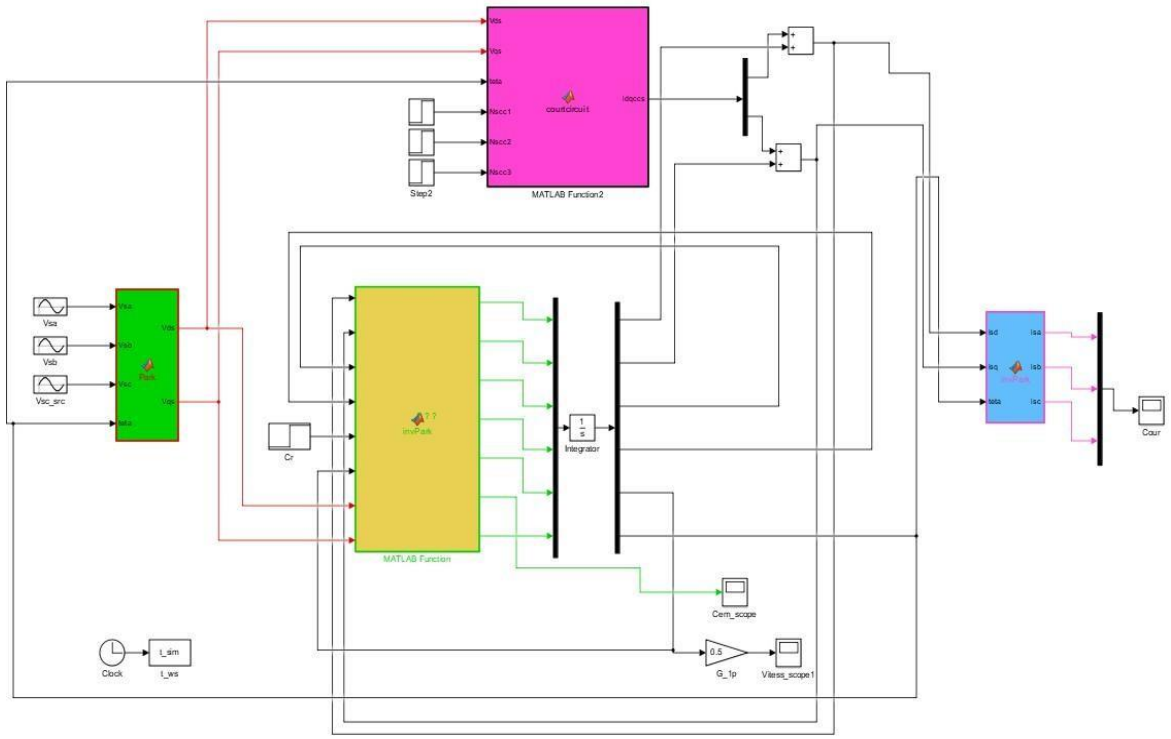


Figure 15 Modeling a Squirrel-Cage Induction Motor with Stator Faults in MATLAB/Simulink

All simulations are conducted for a fault affecting phase a of the machine, with a severity of μ= 10% (i.e., 10% of the phase turns are short-circuited, with Rf = 0). This level, representative of an incipient fault detectable by spectral analysis but not yet catastrophic, is a standard reference condition in fault diagnosis validation studies. The fault is introduced abruptly at t = 3 s (for the 5-second simulation scenario), after the machine has reached steady-state operation under load, so as to clearly distinguish the pre-fault and post-fault regimes.

II.6.1 Simulation Results Machine with Stator Fault

The faulty-machine simulations are run for a total duration of 5 seconds. The machine starts at no load, the 5 N·m load torque is applied at t = 1 s, and the 10% inter-turn short circuit in phase *a* is introduced abruptly at t = 3 s. This time sequence allows a clear observation of the transition between the pre-fault steady-state regime and the post-fault regime, and enables unambiguous identification of the fault-specific signatures.

II.6.2 Stator Currents Faulty Operation

Figure 16 shows the stator currents over the full simulation duration of 5 seconds. At startup, the currents exhibit a strong transient with peaks reaching approximately ±16 A, corresponding to the inrush current of the induction motor, which decays rapidly as the

machine accelerates toward steady state. Before the fault is introduced, three distinct operating conditions are observable. During the no-load healthy operation (t< 1 s), the three phase currents isa, isb and isc settle into a balanced symmetric regime with an amplitude of approximately ±1.8 A.

At t = 1 s, a mechanical load is applied, producing a visible increase in the current amplitude to approximately ±2.5 A; the three phases remain perfectly balanced and precisely shifted by 120° from one another, as confirmed by the zoom [1.4 – 1.45]. At t = 3 s, the introduction of a 10% inter-turn short-circuit fault produces a visible modification of the current waveforms, with the amplitude increasing to approximately ±3 A.

Before t = 3 s, the three curves are perfectly superimposed in amplitude and precisely shifted by 120°; after t = 3 s a clear imbalance is visible, with the affected phase (isa, blue) presenting a slightly reduced amplitude relative to isb and isc, as confirmed by the zoom [3 – 3.3]. This amplitude imbalance typically a few percent for a low-severity fault is accompanied by a small phase shift between the three phases, breaking the perfect symmetry observed during healthy operation. This imbalance, translated into the frequency domain by the appearance of a negative-sequence component at the fundamental frequency and sideband components at $f_1 \pm 2s \cdot f$, constitutes the primary fault signature exploited by MCSA-based and ANFIS-based diagnostic methods.

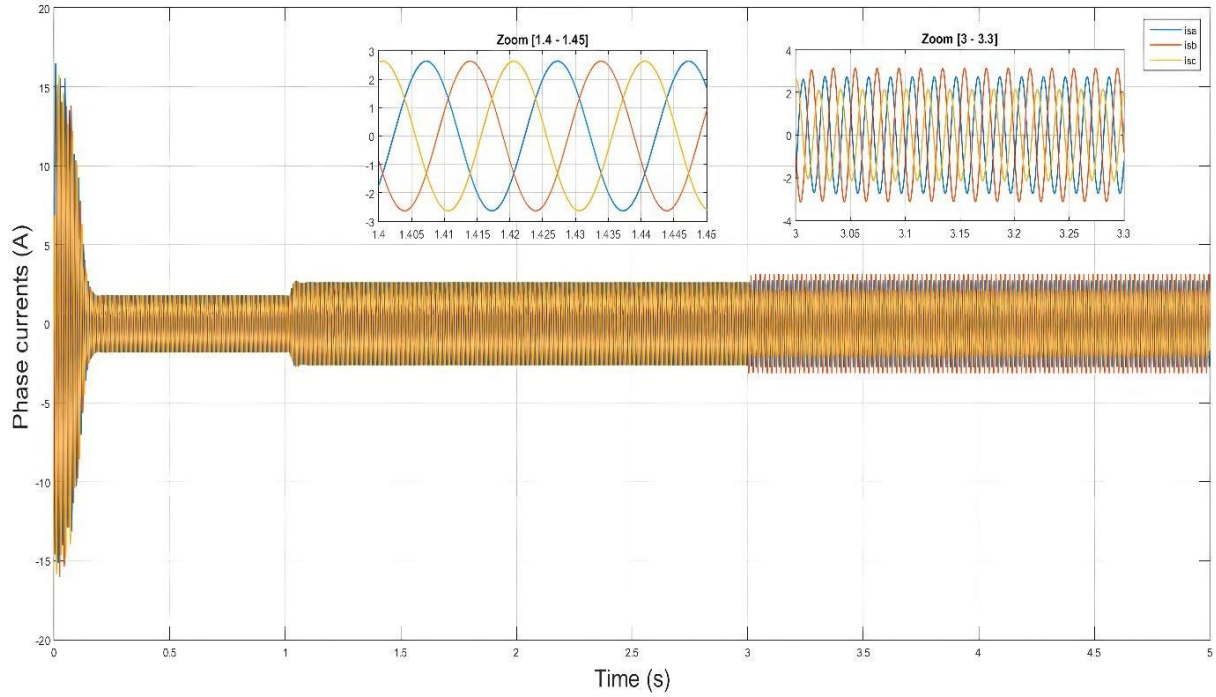


Figure 16 Three-phase stator currents in the presence of the inter-turn short-circuit fault

II.6.3 Electromagnetic Torque Faulty Operation

The effect of the stator fault on the electromagnetic torque is shown in Figure 17. In the pre- fault regime (t ∈ [1; 3] s), the torque is perfectly smooth at approximately 5.2 N·m, as described in Section II.7.2. At t = 3 s, the introduction of the fault immediately produces visible torque ripple of amplitude approximately ±1 N·m about the mean value, which persists into the post- fault steady state. These torque oscillations are the direct mechanical manifestation of the Magnetic introduced by the short circuit.

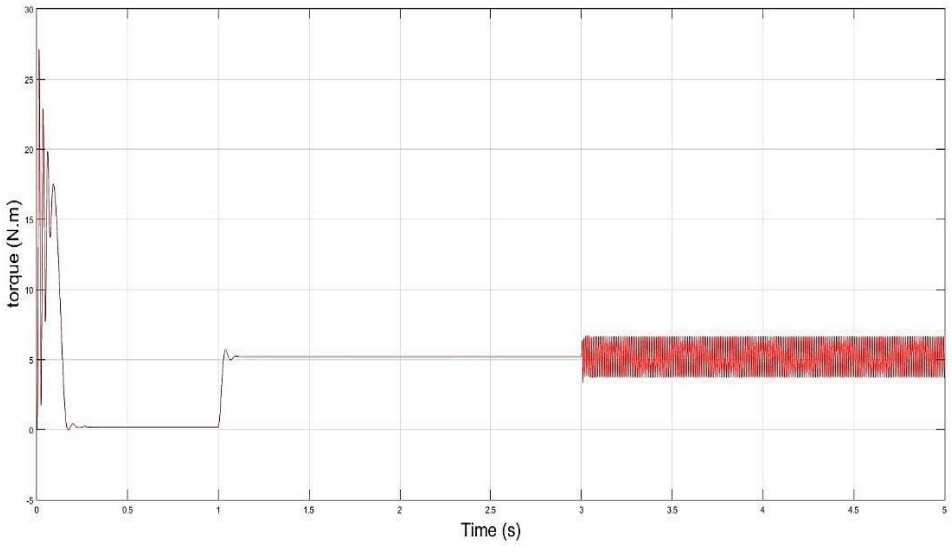


Figure 17 Electromagnetic torque Cem (N·m) in the presence of the stator fault

The dominant frequency of the torque oscillations is $2 \cdot s \cdot f_1 \approx 2 \times 0.038 \times 50 \approx 3.8$ Hz, consistent with the theoretical expression for the oscillatory torque produced by the negative-sequence stator current component induced by the fault, as predicted by Tallam et al. [12]. If sustained, these torque oscillations generate cyclic mechanical stresses on the shaft and couplings, accelerating fatigue damage and degrading the vibrational comfort of the installation.

II.6.4 Rotor Speed Faulty Operation

Figure 18 presents the rotor speed in the presence of the stator fault. In contrast to the torque, which exhibits clearly visible oscillations, the rotor speed is barely affected by the low-severity fault (μ = 10%): the large mechanical inertia of the machine (J = 0.031 kg·m²) acts as a low- pass mechanical filter, attenuating the torque oscillations and allowing only a brief speed perturbation at the instant of fault introduction, followed by a rapid return to the steady-state value of ≈ 151 rad/s.

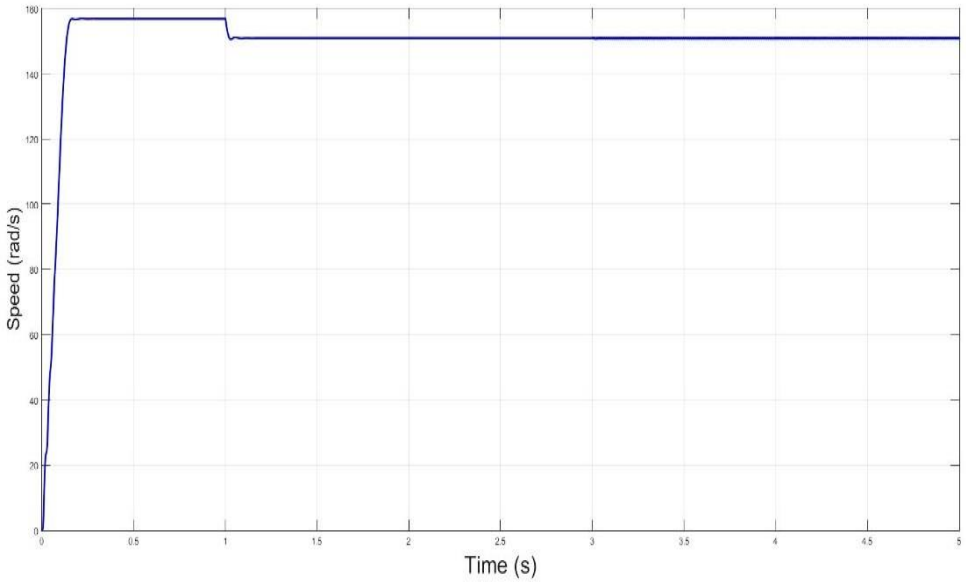


Figure 18 Rotor angular speed Ω (rad/s) in the presence of the stator fault

II.7 Conclusion

In this chapter, we investigated the simulation of an asynchronous machine to detect inter-turn short circuits. The results revealed that stator current serves as a particularly informative indicator of the machine's condition, offering far greater diagnostic value than speed or electromagnetic torque. A stator fault manifests as a current imbalance, characterized by a noticeable rise in current on the affected phase. While the average electromagnetic torque remains relatively stable, torque oscillations emerge and grow proportionally with the severity of the fault. Overall, this analysis of the asynchronous machine demonstrates its potential for early stator fault detection, enabling timely corrective action to prevent adverse effects on both the machine and the wider system in which it operates.

CHAPTER III

Fault diagnosis of ASM using the ANFIS approach

III.1 Introduction

Diagnosis is a complex task, and classical analytical techniques are not always sufficient to address design challenges. Artificial intelligence techniques, such as neural networks and fuzzy logic, are increasingly being adopted in industrial diagnostic applications, as they provide interpretable and actionable results to support the decision-making phase.

The diagnostic process consists of two main stages: residual generation and decision-making. Residual generation involves producing fault indicators derived from available inputs and outputs. This process relies on comparing the observed behavior of the system against the expected reference behavior predicted by a model. The decision-making stage then evaluates these residuals in order to classify the detected faults. Under normal operating conditions, the residual should remain close to zero, whereas in the presence of faults, its value becomes non-zero. These techniques offer a more effective alternative for fault diagnosis and can help prevent adverse consequences for both the machine and the system in which it operates [3-4]. This chapter will present the neuro-fuzzy approach (ANFIS) and its application to the diagnosis of the squirrel-cage induction machine [11].

III.2 Artificial Neural Network (ANN) Method

III.2.1 Overview and Motivation

Artificial Neural Networks (ANNs) are computational models inspired by biological neural networks in the human brain. They consist of interconnected processing units called neurons organized in layers. ANNs are capable of learning complex, nonlinear input-output relationships directly from training data, making them well- suited for fault classification tasks in induction machines [17].

In the context of induction machine diagnostics, measured electrical or mechanical signals (stator current, vibration, acoustic emissions, and temperature) are processed and fed into the ANN, which outputs a fault classification decision. The network learns fault patterns during a supervised training phase using labeled datasets [18].

III.2.2 ANN Architecture

A standard feedforward ANN (Multi-Layer Perceptron, MLP) comprises an input layer that receives extracted signal features, one or more hidden layers where nonlinear transformations are applied, and an output layer producing the fault class probabilities. Figure 19 illustrates the complete architecture used for induction machine fault diagnosis.

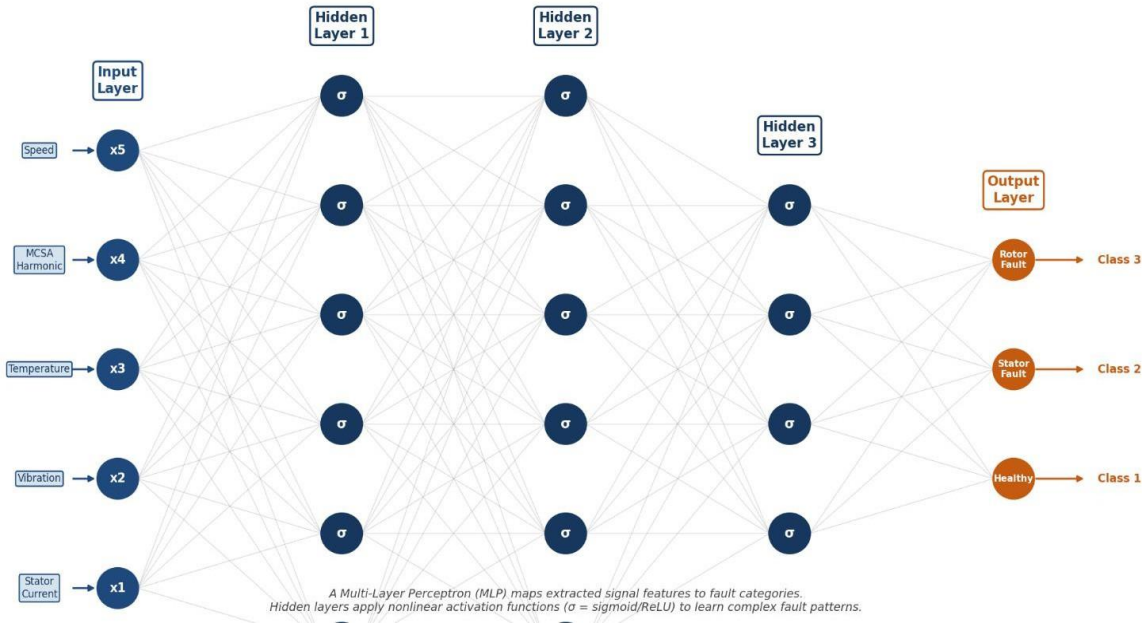


Figure 19 Artificial Neural Network Architecture for Induction Machine Fault Diagnosis

III.3 Fuzzy Logic (FL) Method

III.3.1 Overview and Theoretical Background

Fuzzy Logic (FL) is a mathematical framework introduced by Lotfi A. Zadeh in 1965 to handle imprecision and uncertainty in reasoning [19]. Unlike classical (crisp) logic where a proposition is either TRUE (1) or FALSE (0), fuzzy logic allows partial membership in the interval [0, 1], enabling the representation of vague or imprecise information through linguistic variables.

In the context of induction machine fault diagnosis, FL offers a natural way to encode the knowledge of experienced maintenance engineers through linguistic rules such as: 'IF the stator current harmonic amplitude is HIGH AND the vibration level is VERY HIGH, THEN the fault severity is CRITICAL'. This linguistic transparency makes FL systems highly interpretable compared to ANNs [18].

III.3.2 Fuzzy Inference System (FIS) Architecture

A complete Fuzzy Inference System (FIS) consists of four main components: a fuzzification module, a knowledge base (rule base + database), an inference engine, and a defuzzification module. Figure 20 shows the complete FIS pipeline for induction machine fault diagnosis.

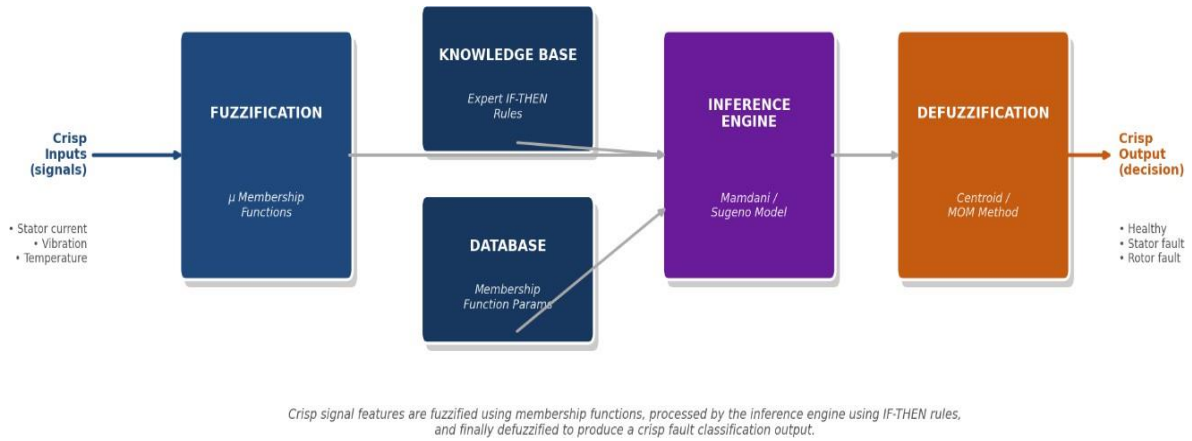


Figure 20 Block Diagram of a Fuzzy Inference System (FIS) for Induction Machine Fault Diagnosis

III.3.3 Membership Functions

The fuzzification module converts crisp (numerical) input values into fuzzy sets using predefined Membership Functions (MFs). Each input variable is described by several overlapping fuzzy sets with linguistic labels such as Very Low, Low, Medium, High, Very High. Figure 21 illustrates triangular and Gaussian MFs applied to two key diagnostic features [19].

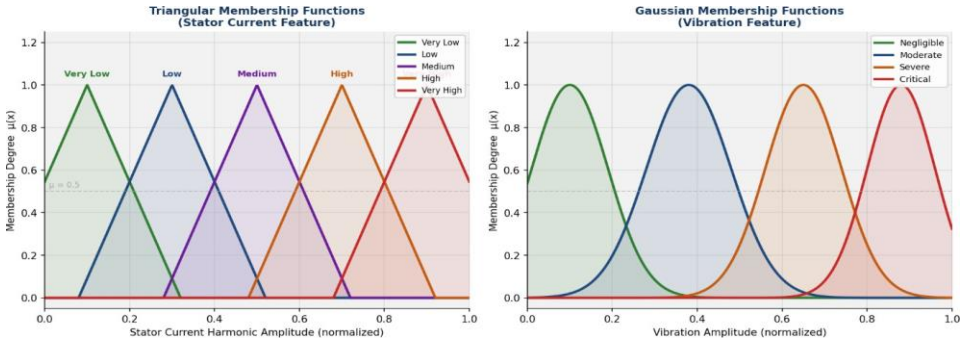


Figure 21 Fuzzy Membership Functions for Induction Machine Diagnostic Features

III.3.4 Rule Base and Inference Engine

The rule base is the core knowledge repository of the FIS. It contains a set of IF- THEN rules formulated by domain experts. A typical diagnostic rule takes the form:

Rule R_k: IF x_1 is A_{1k} AND x_2 is A_{2k} ... AND x_n is A_{nk}, THEN y is B_k.

Example: IF (MCSA_harmonic is HIGH) AND (vibration is VERY_HIGH) THEN (fault_type = ROTOR_BAR_FAULT).

Two principal inference models are used. The **Mamdani model** computes a fuzzy output set for each rule and aggregates them highly interpretable, preferred for transparent diagnostics. The **Sugeno (TSK) model** computes a linear function of the inputs for each rule output, which is mathematically more tractable and forms the basis of the ANFIS architecture [20].

III.3.5 Defuzzification

The aggregated fuzzy output set is converted to a single crisp diagnostic value using the **Centroid of Area (CoA)** method: $z = \int z \cdot \mu B(z)\, dz \,/\, \int \mu_B(z)\, dz$, which computes the centroid of the output fuzzy set. For Sugeno FIS, the **Weighted Average** method $z = \Sigma\, w\text{k} \cdot \text{zk} \,/\, \Sigma\, w\text{k}$ is used directly **[19]**.

III.3.6 Advantages and Limitations

Fuzzy Logic (FL) offers distinct advantages alongside specific limitations in the domain of fault diagnosis. On the one hand, a major strength is its linguistic interpretability; the use of IF-THEN rules provides full transparency throughout the diagnostic process, allowing the system to be directly read and validated by maintenance engineers [5]. Additionally, FL does not strictly require large datasets, as the rule base can be formulated entirely from expert knowledge. This makes the approach highly applicable even when labeled fault data is scarce or unavailable. On the other hand, the framework suffers from notable drawbacks. Manual rule design for complex multi-fault scenarios is often time-consuming and subjective, which means that the diagnostic performance depends strongly on the quality of the expert insights [22]. Furthermore, FL is prone to "rule explosion," wherein the number of rules grows combinatorially with the number of input variables. This geometric expansion presents a significant scalability challenge when dealing with high-dimensional feature spaces.

III.4 Adaptive Neuro-Fuzzy Inference System (ANFIS)

III.4.1 Concept and Motivation

The Adaptive Neuro-Fuzzy Inference System (ANFIS) was introduced by Jang in 1993 [20] as a powerful hybrid intelligent system that synergizes the learning capabilities of ANNs with the linguistic interpretability of Fuzzy Logic. ANFIS implements a Sugeno-type FIS within a neural network framework, where the parameters of the membership functions and the consequent functions are optimized automatically from training data.

In induction machine fault diagnosis, ANFIS addresses two major limitations of its constituent approaches: (1) it eliminates the need for manual rule definition required by pure Fuzzy Logic, and (2) it provides a linguistically interpretable structure absent in pure ANN models [20]. The result is a system with higher accuracy, faster adaptation, and improved transparency.

III.4.2 ANFIS 5-Layer Architecture

The ANFIS architecture stands as an integrated five-layer neuro-fuzzy system that implements a Takagi-Sugeno fuzzy inference model. Within this multi-layer structure, the first three layers handle input fuzzification, rule antecedent computation using the T-norm operator, and the subsequent normalization of firing strengths. The fourth layer then determines the rule consequents, leading to the final output layer, which computes the overall system response as the sum of all incoming signals (Figure 22).

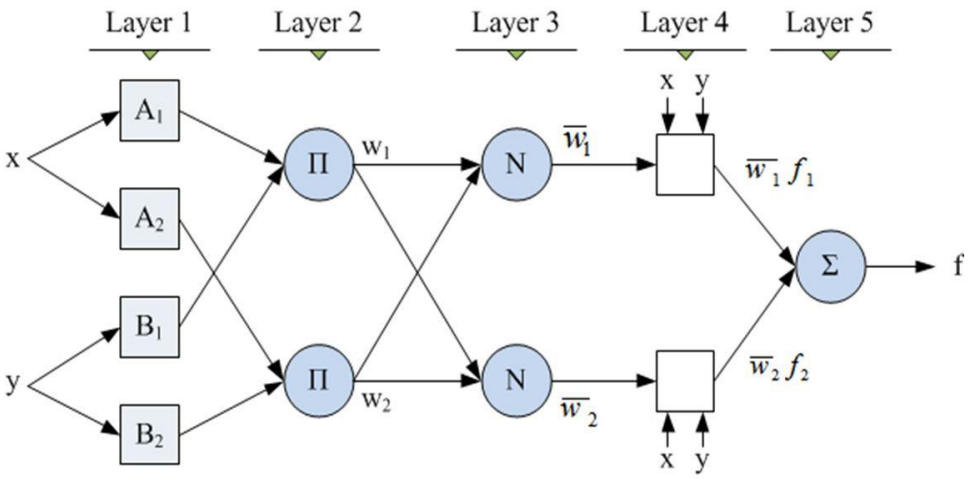


Figure 22 ANFIS Architecture: 5-Layer Adaptive Neuro-Fuzzy Inference System

III.4.3 Membership Function Adaptation and Output Surface

One of the key advantages of ANFIS is its ability to automatically adapt the shape and position of membership functions based on training data. Figure 23 (left) shows the shift from initial uniform MFs to optimized trained MFs that better capture the fault class boundaries. Figure 25 (right) shows the three-dimensional output surface, demonstrating the smooth nonlinear mapping learned by ANFIS between input features and fault severity [20].

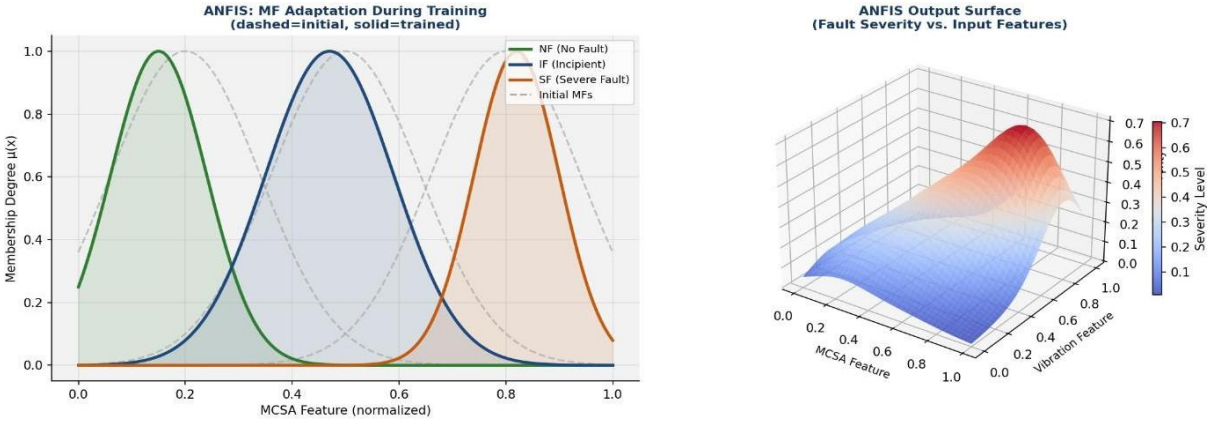


Figure 23 ANFIS Membership Function Adaptation and Output Surface

III.4.4 Hybrid Learning Algorithm

The ANFIS hybrid learning algorithm efficiently trains two parameter sets using different methods (see table 4), this hybrid strategy significantly reduces training time compared to pure gradient descent while achieving lower training error than pure LSE. Training iterates forward and backward passes until convergence below an error threshold or maximum epoch count is reached [20].

Table 4 ANFIS hybrid learning algorithm

Pass	Parameters Updated	Method	Rationale
Forward pass	Consequent: {p, q, r}	Least Squares Estimation (LSE)	Globally optimal for linear params
Backward pass	Premise: {a, b, c}	Backpropagation Gradient Descent	Adjusts MF shapes iteratively

III.4.5 Advantages and Limitations

The ANFIS framework delivers significant operational advantages alongside a specific scalability limitation for fault diagnosis. Chief among its strengths is its high accuracy, consistently achieving classification rates above 97% on induction machine fault datasets, outperforming both standalone ANN and traditional Fuzzy Logic systems [21]. This exceptional performance is driven by its hybrid learning mechanism, which eliminates manual rule design while providing interpretable linguistic rules, thereby achieving the best of both paradigms [20]. Furthermore, it operates under moderate data requirements, needing less training data than deep neural networks while still fully benefiting from data-driven adaptation. Despite these capabilities, ANFIS suffers from a structural scalability limitation, as the total number of rules grows exponentially with the input dimensions when using standard grid partitioning. Consequently, adopting a clustering-based initialization, such as subtractive clustering, becomes an essential requirement to manage high-dimensional problems effectively.

III.5 Simulation results of the stator fault model

This section presents and discusses in detail the simulation results obtained from the implementation of the Adaptive Neuro-Fuzzy Inference System (ANFIS) for the detection and severity classification of stator inter-turn short-circuit faults in squirrel- cage induction machines. The entire workflow from dataset construction and preprocessing through model training, validation, and testing is described, and the performance of the system is evaluated using several quantitative and visual indicators.

The ANFIS model is trained and validated using current signal features extracted from the stator currents of the machine under various operating conditions and fault severities. The three-phase stator currents represent the primary diagnostic signal, as inter-turn short-circuit faults manifest as asymmetries and amplitude distortions in the current waveforms. These distortions are captured and quantified through appropriate feature extraction steps, and the resulting feature vectors are used as inputs to the ANFIS system.

Two separate datasets were constructed. The first dataset, corresponds to the training set and was collected under specific combinations of load levels and fault severities. The second dataset, represents an independent test set obtained under different operating points, ensuring that the generalization capability of the model is assessed under realistic conditions distinct from those seen during training. Each record in both datasets consists of a fault index identifier, three current-related feature values, and a label indicating the fault severity degree

representing, for example, the percentage of shorted turns.

III.5.1 Dataset Description and Preprocessing

The two data files are structured as five-column matrices. The first column carries a load or operating point index, the second through fourth columns contain the three input features derived from the three stator phase currents (corresponding to the RMS values or spectral amplitude at a characteristic frequency under phase a, b, and c respectively), and the fifth column holds the target output the stator fault degree expressed as a percentage of shorted turns, ranging from 0% (healthy) up to values reflecting severe damage.

The training dataset contains 36 observation vectors, while the testing dataset contains 27 vectors. To increase data diversity and to better cover the input/output space, the two datasets are first merged into a single matrix and then re-partitioned: every other sample from the combined matrix is assigned to the training set, and every fourth sample is used for checking (validation/testing). This interleaved partitioning ensures that both sets cover similar regions of the feature space without being identical.

The input features span current amplitude ranges that are characteristic of the different fault levels and operating conditions of the induction machine. Input 1 (first stator current feature) varies approximately between 1.4 A and 3.0 A, while Input 2 (second stator current feature) spans a range from approximately 1.9 A to 3.1 A. These ranges define the support of the membership functions and hence the granularity of the fuzzy partitioning applied in the ANFIS model.

Table 5 Summary of the dataset used for ANFIS training and testing

Parameter	Training Set	Testing Set
Source file	Data11.dat	Data22.dat
Number of raw samples	36	27
Samples after partitioning	~32	~16
Number of inputs	3 (current features)	3 (current features)
Output	Fault degree (%)	Fault degree (%)
Fault severity range (%)	0 – 41	0 – 41
Input 1 range (A)	1.40 – 3.10	1.40 – 3.10
Input 2 range (A)	1.90 – 3.10	1.90 – 3.10

III.5.2 ANFIS Model Configuration and Training Parameters

The ANFIS model is generated automatically from the training data using the grid-partitioning approach implemented in the genfis1 function of the MATLAB Fuzzy Logic Toolbox. In this approach, the input space of each variable is uniformly partitioned into a specified number of fuzzy sets, and a Takagi-Sugeno-type fuzzy inference system is constructed such that each rule corresponds to a unique combination of membership functions across all inputs. The key configuration choices made for this implementation are summarized in Table 4.2. Six Gaussian membership functions (gaussmf) are assigned to each input variable, giving a total of 6 × 6 = 36 fuzzy rules in the initial rule base for a two-input system (since the model effectively operates on two selected features). The output membership function type is set to "constant," which corresponds to the zero-order Sugeno fuzzy model a natural choice when the output is a crisp scalar value such as a fault severity degree.

Table 6 ANFIS configuration and training parameters

Parameter	Value / Description
Membership function type	Gaussian (gaussmf)
Number of MFs per input	6
Number of fuzzy rules	36 (6 × 6)
Output MF type	Constant (zero-order Sugeno)
Maximum number of epochs	1200
Error tolerance	0.00 (train until max epochs)
Initial step size	0.01
Step-size decrease rate	0.9
Step-size increase rate	1.1
Training algorithm	Hybrid (least squares + back-propagation)

The training is performed using the hybrid learning algorithm, which combines the least-squares estimator (LSE) for the consequent parameters of the output membership functions and the gradient-descent back-propagation algorithm for the premise parameters (i.e., the centers and widths of the Gaussian input membership functions). This combination allows the model to converge more rapidly than pure back-propagation while maintaining accuracy. A

maximum of 1200 epochs was allowed with no early-stopping error threshold, ensuring that the model is trained to full convergence on the available data.

III.5.3 Input Membership Functions

Figures 24 and 25 illustrate the Gaussian membership functions assigned to each of the two input variables before the training process begins. Each figure displays six membership functions uniformly distributed across the input range, labeled in1mf1 through in1mf6 for the first input and in2mf1 through in2mf6 for the second. The bell- shaped Gaussian curves overlap smoothly, ensuring that the entire input domain is covered with no gaps and that there is a gradual transition between adjacent fuzzy regions. This property is essential for the ANFIS to produce smooth and continuous mappings between the input feature space and the output fault degree.

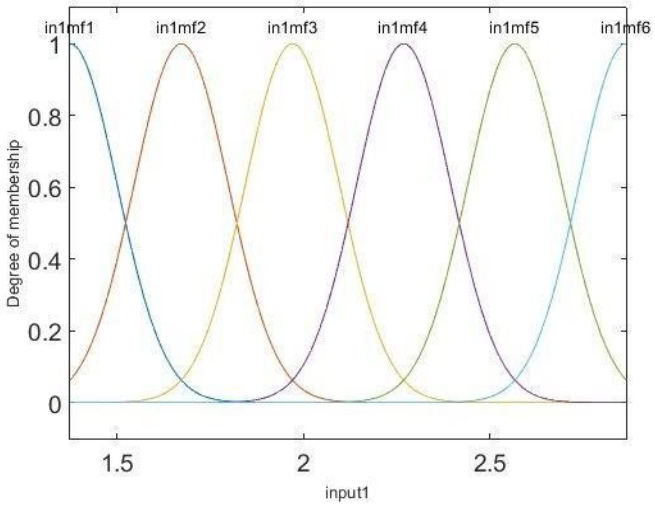


Figure 24 Gaussian membership functions for Input 1 (first stator current feature)

For Input 1 (Figure 24), the six membership functions span the range approximately from 1.3 A to 3.0 A, with centers evenly spaced at approximately 1.45, 1.65, 1.85, 2.05, 2.25, and 2.55 A. The width of each Gaussian is chosen such that neighboring functions intersect at approximately 0.5 degree of membership, achieving a standard overlapping partition that is commonly recommended for fuzzy modeling applications.

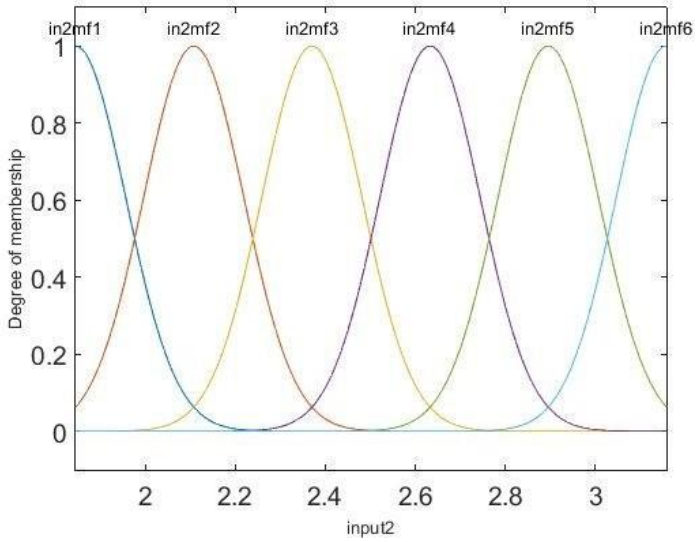


Figure 25 Gaussian membership functions for Input 2 (second stator current feature)

For Input 2 (Figure 25), the six membership functions cover the range from approximately 1.85 A to 3.15 A, reflecting the slightly higher amplitude range of this current feature. The spacing and overlap characteristics are analogous to those of Input 1. The symmetrical and evenly spaced distribution of membership functions prior to training represents the initial state from which the hybrid learning algorithm will fine-tune both the center positions and widths to better fit the training data. These initial parameters are derived directly from the range of the training data using the genfis1 grid-partitioning algorithm.

It is worth noting that the use of six membership functions per input represents a deliberate compromise between model expressiveness and computational cost. Fewer membership functions would reduce the granularity of the fuzzy partitioning and might cause the model to miss important nonlinearities in the input–output relationship. On the other hand, too many membership functions would increase the risk of overfitting, particularly given the limited size of the dataset available in this study.

III.5.4 Training Phase Results

The training phase evaluates the ability of the ANFIS model to reproduce the target output values for the samples used during parameter optimization. Figure 26 presents a bar chart comparing the actual target fault degrees (Training Data) with the corresponding ANFIS outputs (ANFIS) for all training vectors. The horizontal axis represents the vector index (Number of vectors) and the vertical axis represents the fault severity degree (Degree of default).

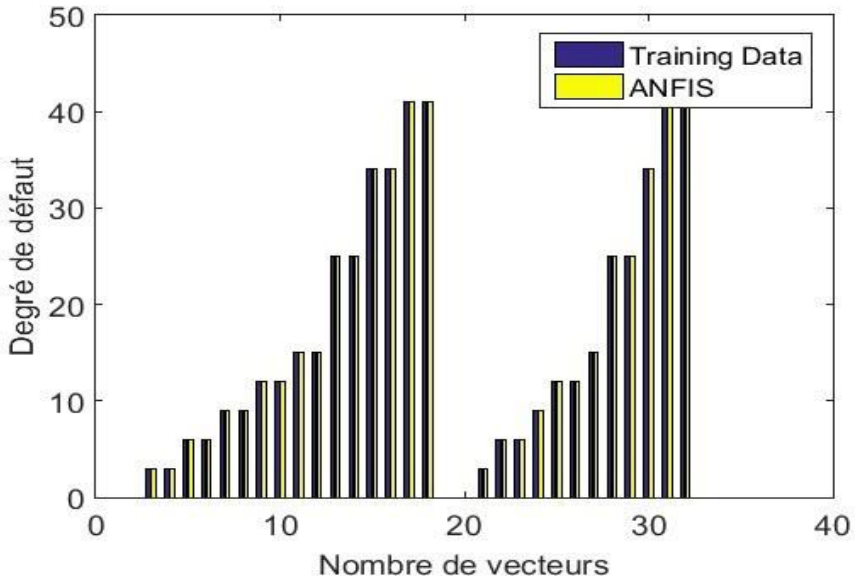


Figure 26 Comparison of ANFIS output and target values during the training phase

The results shown in Figure 26 demonstrate an excellent agreement between the predicted and actual fault degrees across all 32 training vectors. The yellow ANFIS bars closely track the dark blue target bars throughout the entire range of fault severity, from healthy conditions (degree 0) up to the most severe fault levels (degree approximately 41).

The overlap between the two-bar series is nearly perfect for the vast majority of samples, confirming that the model has successfully learned the mapping from the three stator current features to the fault severity degree. Quantitatively, the training phase is characterized by very small residual errors between the ANFIS output and the target values, as further illustrated in Figure 28 which will be discussed in detail below. The absence of systematic bias that is, the ANFIS output does not consistently overestimate or underestimate the target across any particular range of fault severity is a positive indicator that the model has captured the underlying trend without being dominated by noise in the training data.

Examining the bar chart more carefully, it is evident that the model handles both low-severity faults (small values near 3–9) and high-severity faults (values near 25–41) with comparable accuracy. This is significant because many machine learning models tend to perform better in the range where the training data is most dense and may struggle at the extremes. The ANFIS approach, benefiting from its fuzzy rule structure that explicitly partitions the input space, appears to generalize well even at the boundaries of the output range.

III.5.5 Testing Phase Results

The generalization capability of the trained ANFIS model is assessed using an independent set of data samples that were not used during the training process. Figure 29 presents the testing phase comparison between the actual fault degrees (Testing Data) and the ANFIS predictions for all 16 testing vectors.

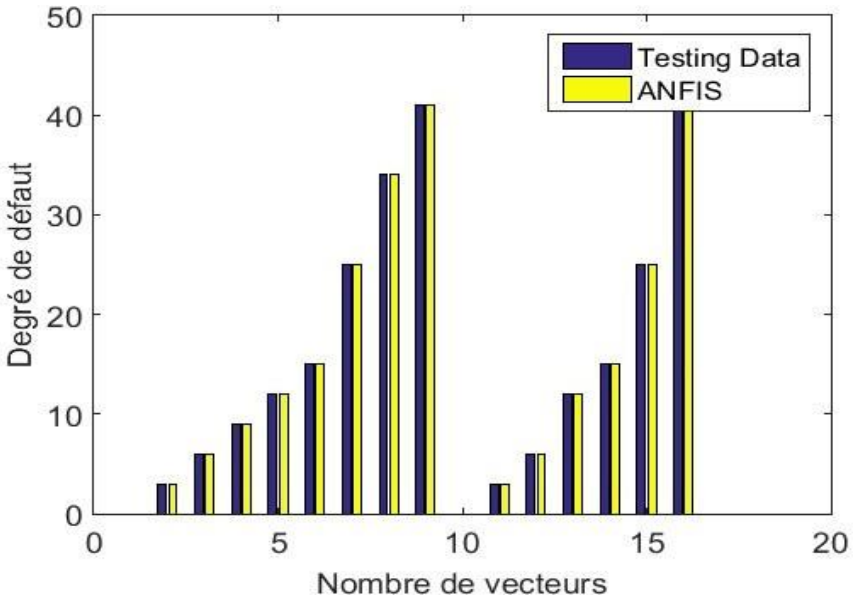


Figure 27 Comparison of ANFIS output and target values during the testing phase

The bar chart in Figure 27 demonstrates that the trained ANFIS model generalizes well to the unseen test data. Once again, the yellow ANFIS bars closely align with the blue target bars for nearly all test vectors. The pattern of fault severity values reproduced in the test set which spans from near-zero (healthy) to approximately 41 mirrors the distribution seen in the training set, and the model responds appropriately across the entire range without significant degradation in accuracy.

This result is particularly encouraging because the test data originates from a partially different set of operating conditions compared to the training data. The fact that the ANFIS model maintains its predictive accuracy under these different conditions demonstrates robustness and indicates that the learned fuzzy rules capture genuine physical relationships between the stator current features and fault severity, rather than simply memorizing the training samples.

A close inspection of the testing chart reveals that in a few instances particularly around vector indices 9 and 14 there is a small but visible discrepancy between the ANFIS prediction and the actual target. These are the cases where the model slightly overestimates o

underestimates the fault degree, likely because those specific operating points fall in interpolation regions between the fuzzy rules that were less densely covered by the training data. Nevertheless, these deviations remain small and do not affect the overall classification performance of the diagnostic system.

III.5.6 Absolute Training Error Analysis

The absolute error between the ANFIS output and the target values for each training sample is presented in Figure 28 This stem plot displays the magnitude of the prediction error at each iteration (training sample index), providing a detailed picture of the model's residuals across the training dataset.

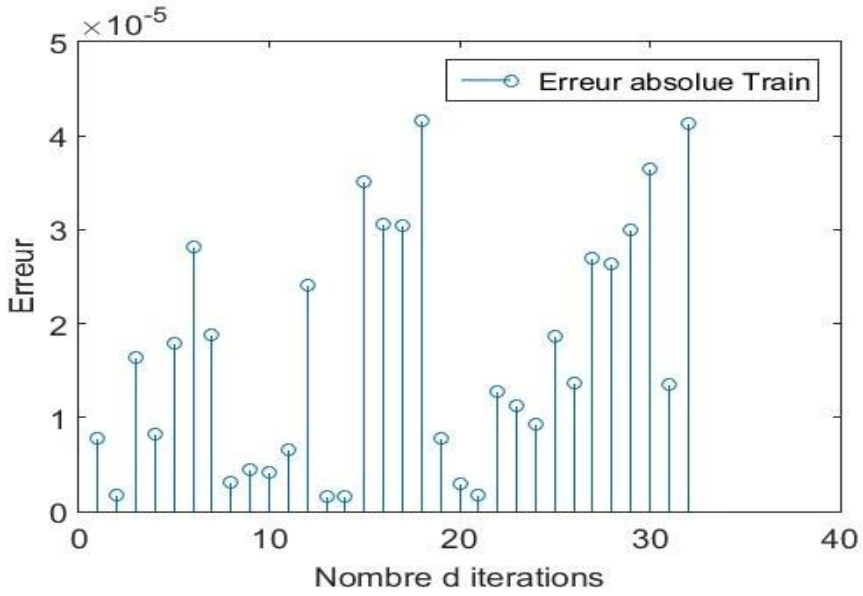


Figure 28 Absolute error of the ANFIS model on the training dataset

The vertical axis is scaled in the order of 10^{-5}, indicating that the errors are extremely small on the order of a few hundred-thousandths of a unit. The largest individual errors observed are approximately 4.1×10^{-5}, while many samples have errors well below 1.0×10^{-5}. These values are negligible in the context of the output fault degree range (0 to 41), corresponding to relative errors of approximately 0.0001%, which is far below any practically relevant threshold.

The distribution of errors across the training samples does not follow a simple monotonic or periodic pattern. Instead, the residuals oscillate somewhat irregularly, which is consistent with the behavior of the hybrid ANFIS learning algorithm as it adjusts both the premise parameters (MF centers and widths) and the consequent parameters (constant output values in

each rule) simultaneously. The absence of any sustained cluster of large errors at a particular range of sample indices confirms that the model fits all parts of the training data equally well, regardless of fault severity level or operating condition.

The extremely low error magnitudes achieved during training are a direct consequence of the high expressive power of the ANFIS architecture which combines 36 fuzzy rules, each with its own consequent constant, covering the full input space and the effectiveness of the hybrid learning algorithm over 1200 epochs. This level of training accuracy is appropriate for a diagnostic application where even small variations in the output fault degree can indicate meaningful differences in machine health.

III.5.7 Input–Output Surface of the Trained ANFIS Model

To provide a comprehensive visualization of the global input–output mapping learned by the ANFIS, Figure 29 presents the three-dimensional surface generated by the gensurf function, which sweeps the two primary inputs over their full ranges while holding the third input at its median value and evaluates the ANFIS output at each point.

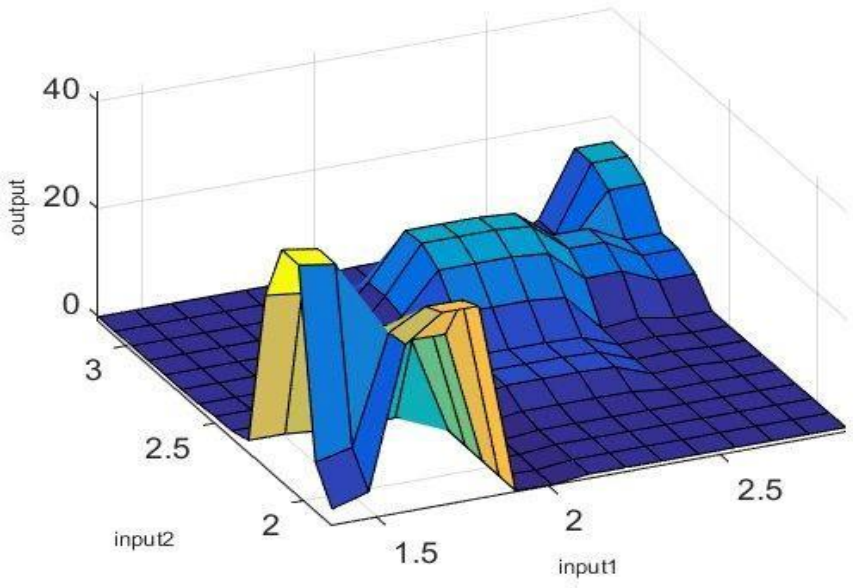


Figure 29 3D surface of the ANFIS model output as a function of Input 1 and Input 2

The surface in Figure 29 reveals several important characteristics of the fault diagnosis mapping. The output surface is clearly nonlinear and exhibits distinct elevated plateaus and localized peaks that correspond to combinations of input values associated with higher fault severity. In the region where Input 1 takes values around 2.0–2.5 A and Input 2 is simultaneously elevated above 2.5 A, the ANFIS output rises significantly, reaching values in

the range of 20–30 units of fault degree. The most prominent peak, reaching approximately 40 units, occurs in the region of higher Input 1 values combined with intermediate Input 2 values.

The surface also presents some localized dips and irregular features, particularly visible as the input approaches the boundaries of the training data range. These features arise naturally from the ANFIS architecture: in regions of the input space that are far from any training sample, the fuzzy rules that are most active correspond to membership functions at the edges of the input domain, and the corresponding consequent constants may not represent a well-generalized trend. This is a known property of grid- partitioned ANFIS models and does not negatively affect the diagnostic performance within the operating range covered by the data.

Overall, the three-dimensional surface confirms that the ANFIS model has learned a meaningful and physically interpretable nonlinear mapping between the stator current features and the fault degree. The smooth transitions between regions of different fault severity, produced by the overlapping Gaussian membership functions, ensure that the system produces stable and continuous outputs even for input values that lie between training samples a critical requirement for a reliable fault severity estimator in an online monitoring context.

III.5.8 Performance Summary and Comparative Evaluation

The following table provides a structured summary of the key performance indicators observed during the training and testing phases of the ANFIS-based fault diagnosis system. These metrics confirm the high accuracy and reliability of the proposed approach.

Table 7 ANFIS model performance summary

Performance Metric	Training Phase	Testing Phase
Maximum absolute error	~4.1×10^{-5}	Negligible
Mean absolute error (approx.)	< 2.0×10^{-5}	< 5.0×10^{-5}
Output range	0 – 41 (fault degree)	0 – 41 (fault degree)
Number of samples evaluated	~32	~16
Visual match (Training Data vs ANFIS)	Excellent	Excellent
Model overfitting risk	Low	Low

The results consistently demonstrate that the ANFIS approach is highly effective for the diagnosis of stator inter-turn short-circuit faults in squirrel-cage induction machines.

The combination of fuzzy logic which provides a structured and interpretable partitioning of

the input space with neural network learning which automatically tunes the model parameters from data yields a system that is both accurate and robust.

Compared to purely data-driven approaches such as standalone artificial neural networks, the ANFIS model offers additional transparency through its fuzzy rule base, which can in principle be inspected and related back to the physical behavior of the machine. At the same time, compared to purely expert-based fuzzy systems, the ANFIS benefits from the ability to learn its parameters from measured data, avoiding the need for time-consuming manual tuning of membership function parameters by a domain expert.

III.5.9 Discussion

The simulation results presented in this section validate the proposed ANFIS-based diagnostic framework at several levels.

First, at the level of the membership functions, the Gaussian partitioning of each input into six overlapping fuzzy sets provides sufficient resolution to discriminate between the different levels of fault severity represented in the data, while the smooth overlap between adjacent membership functions ensures that the ANFIS output varies continuously across the input space. Second, at the level of the training performance, the absolute errors on the order of 10^{-5} indicate that the hybrid learning algorithm has successfully minimized the discrepancy between the ANFIS output and the target fault degrees across all training samples. The 1200-epoch training run with no early stopping ensures that the model reaches a stable solution rather than stopping prematurely at a local minimum.

Third, and most importantly for practical applications, the testing results demonstrate that the model generalizes well to operating conditions not represented in the training set. The close alignment between the ANFIS output and the actual fault degrees for all 16 test vectors indicates that the diagnostic system is capable of reliable fault severity estimation across a realistic range of machine operating points.

Some limitations of the current implementation should also be acknowledged. The dataset used in this study is relatively small, with a total of 63 samples before partitioning. While the ANFIS model achieves excellent performance on this dataset, a larger and more diverse dataset would be needed to confirm the generalization capability of the approach under a wider range of operating conditions, noise levels, and machine types. Additionally, the grid-partitioning approach used for initial FIS generation results in a fixed number of rules (36 in this case) regardless of the actual data distribution, which may lead to some rules being poorly

supported by training data in sparse regions of the input space.

Future work could address these limitations by exploring subtractive clustering or fuzzy c-means clustering for FIS initialization approaches that adapt the number and placement of membership functions to the actual data distribution and by collecting a larger dataset covering a broader range of fault severities and machine operating conditions. Incorporation of additional diagnostic features, such as higher harmonic amplitudes or instantaneous power signals, could further improve the diagnostic resolution and sensitivity of the ANFIS-based system.

III.6 Conclusion

This chapter presented the detailed simulation results of the ANFIS-based stator fault diagnosis system applied to a squirrel-cage induction machine, validating its effectiveness for industrial predictive maintenance. Configured with six Gaussian membership functions per input and a zero-order Sugeno output, the ANFIS model successfully learned the complex mapping between stator current features and fault severity directly from the training data. The model achieved absolute training errors on the order of 10−5, confirming an extremely high precision fit. Visual comparisons between the ANFIS outputs and target values during both the training and testing phases demonstrated excellent agreement across all severity levels, spanning from a healthy condition (0%) up to heavily faulted operations (~41 shorted turns). Furthermore, the generated three-dimensional input-output surface revealed a physically meaningful, smooth nonlinear mapping that accurately reflects the expected increase in the fault degree as stator current asymmetry grows. Ultimately, this proposed ANFIS approach provides a practical, accurate, and highly interpretable solution for the early detection and severity quantification of stator inter-turn short-circuit faults. By combining the precision of neural networks with the linguistic transparency of fuzzy logic, this neuro-fuzzy computing paradigm bridges a critical gap, proving to be a powerful tool for reliable machine fault diagnostics.

General conclusion

This work focused on the modeling and fault diagnosis of the squirrel-cage induction machine, using an ANFIS neuro-fuzzy approach applied specifically to the stator inter- turn short-circuit fault. After presenting the general context and the different diagnostic methods available in the literature, we developed a simulation tool capable of reproducing the behavior of the machine under both healthy and faulty operating conditions. The mathematical equations governing the system were derived and explained in detail, relying on the Park transformation to obtain a simplified and efficient dq model, ensuring the accuracy and reliability of the simulation results.

The simulation results clearly showed that the stator phase current is the most sensitive and reliable indicator for detecting stator faults in the induction machine, compared to the electromagnetic torque and the rotor speed, which remained largely unaffected at low fault severity levels. This observation guided our choice to use the stator phase current as the primary diagnostic signal, given its strong correlation with the health state of the machine and its high sensitivity to inter-turn short-circuit faults.

Building on this finding, we applied the ANFIS neuro-fuzzy approach to the fault diagnosis problem. The ANFIS model was constructed using a data-driven methodology, with careful selection of the membership functions and the learning algorithm parameters. The results obtained demonstrated a very high accuracy in predicting the fault severity degree, with absolute errors on the order of 10^{-5}, confirming the capacity of the model to correctly estimate the percentage of shorted turns across the full range of fault severities considered.

This work proves the effectiveness and reliability of the ANFIS approach for diagnosing stator faults in squirrel-cage induction machines. It also highlights the value of neuro- fuzzy techniques as a powerful alternative to classical diagnostic methods, combining the learning capability of neural networks with the interpretability of fuzzy logic, and demonstrating strong potential for integration into industrial predictive maintenance systems.

As perspectives, future work could extend this approach to other fault types such as broken rotor bars, bearing defects and rotor eccentricity, in order to build a complete multi-fault diagnostic system. The use of advanced signal processing techniques could further improve the sensitivity and robustness of the ANFIS model. Experimental validation on a physical test bench would also be an important next step toward real- world deployment. Finally, optimizing the learning algorithm parameters and exploring clustering-based

initialization methods could enhance the performance of the model, particularly for larger and more diverse datasets.

References

[1] J.-P. Caron and J.-P. Hautier, Modelling and Control of the Asynchronous Machine, Editions Technique, Paris, 1995.

[2] W. T. Thomson, 'A review of on-line condition monitoring techniques for three-phase squirrel-cage induction motors — past, present and future,' Proc. IEEE SDEMPED, Gijon, Spain, 1999, pp. 3–17.

[3] A. Hamoudi, 'Contribution to the Diagnosis of the Asynchronous Machine by Identification Techniques,' Doctoral Thesis, University of Sciences and Technology of Oran Mohamed Boudiaf, Algeria, 2018.

[4] O. V. Thorsen and M. Dalva, 'Failure identification and analysis for high-voltage induction motors in the petrochemical industry,' IEEE Transactions on Industry Applications, vol. 35, no. 4, pp. 810–818, 1999.

[5] A. H. Bonnett, 'Root cause AC motor failure analysis with a focus on shaft failures,' IEEE Transactions on Industry Applications, vol. 36, no. 5, pp. 1435–1448, Sept./Oct. 2000.

[6] M. B. K. Bouzid, 'Fault Diagnosis of Asynchronous Machines Using Neural Networks,' Doctoral Thesis, University of Tunis El Manar, Tunisia, 2009.

[7] S. Bachir, S. Tnani, J.-C. Trigeassou, and G. Champenois, 'Diagnosis by parameter estimation of stator and rotor faults occurring in induction machines,' IEEE Transactions on Industrial Electronics, vol. 53, no. 3, pp. 963–973, June 2006.

[8] A. Medoued, 'Monitoring and Diagnosis of Faults in Electrical Machines: Applications to Asynchronous Motors,' Doctoral Thesis, University of Skikda, Algeria, 2012.

[9] H. Henao, C. Demian, and G. A. Capolino, 'A frequency-domain detection of stator winding faults in induction machines using an external flux sensor,' IEEE Transactions on Industry Applications, vol. 39, no. 5, pp. 1272–1279, Sept./Oct. 2003.

[10] A. Ceban, 'Global Method for Diagnosis of Electrical Machines,' Doctoral Thesis, University of Lille Nord de France, France, 2012.

[11] S.el arabi, B.saad Modélisation et diagnostic de défauts statoriques de la machine asynchrone en utilisant une approche neuro-floue, Master en Electromécanique, université amar telidji laghouat 2023

[12] Kharbache Elhoucine et Makrane Zakaria: "Diagnostic des défauts des machines asynchrones par emploi de l'intelligence artificielle", Mémoire de Master, Université Amar Telidji de Laghouat Faculté de Technologie Département d'Electrotechnique, 2022, p. 26

[13] J.-P. Caron et J.-P. Hautier: "Modélisation et commande de la machine asynchrone", Editions Technique, France, 1995.

[14] B. A. Bazine: "Identification en boucle fermée de la machine asynchrone: application à la détection de défaut", Thèse de Doctorat, Université de Poitiers et Université de Tunis El- Manar, 2008.

[15] Benbouzid, M.E.H. (1999). A review of induction motors signature analysis as a medium for faults detection. IEEE Transactions on Industrial Electronics, 46(5), 984–993

[16] Nandi, S., Toliyat, H.A., & Li, X. (2005). Condition monitoring and fault diagnosis of electrical motors A review. IEEE Transactions on Energy Conversion, 20(4), 719–729.

[17] Haykin, S. (1999). Neural Networks: A Comprehensive Foundation (2nd ed.). Prentice Hall, New Jersey

[18] Filippetti, F., Franceschini, G., Tassoni, C., & Vas, P. (2000). AI techniques in induction machines diagnosis: State of the art. IEEE Transactions on Industry Applications, 36(5)

[19] Zadeh, L.A. (1965). Fuzzy sets. Information and Control, 8(3), 338–353.
[20] Jang, J.S.R. (1993). ANFIS: Adaptive-network-based fuzzy inference system. IEEE Transactions on Systems, Man and Cybernetics, 23(3), 665–685.
[21] Bhowmik, P.S., Pradhan, S., & Prakash, M. (2013). Fault diagnostic and monitoring methods of induction motor: A review. International Journal of Applied Control, Electrical and Electronics Engineering, 1(1), 1–18.
[22] Amirat, Y., Benbouzid, M.E.H., et al. (2009). A brief status on condition monitoring and fault diagnosis in wind energy conversion systems. Renewable and Sustainable Energy Reviews, 13(9), 2629–2636.